

## Article

# Probe-Sonicated Synthesis of CuO–ZnO Hybrid Nanocomposite for Photocatalytic and Supercapacitor Applications

Amal BaQais <sup>1</sup>, Mir Waqas Alam <sup>2,\*</sup>, Mohd Farhan <sup>3</sup>, Ghazala Muteeb <sup>4</sup>, Nassiba Allag <sup>5</sup> and Shehla Mushtaq <sup>6</sup>

<sup>1</sup> Department of Chemistry, College of Science, Princess Nourah Bint Abdulrahman University, Riyadh 11671, Saudi Arabia; aabaqeis@pnu.edu.sa

<sup>2</sup> Department of Physics, College of Science, King Faisal University, Al-Ahsa 31982, Saudi Arabia

<sup>3</sup> Department of Basic Sciences, Preparatory Year Deanship, King Faisal University, Al-Ahsa 31982, Saudi Arabia; mfarhan@kfu.edu.sa

<sup>4</sup> Department of Nursing, College of Applied Medical Science, King Faisal University, Al-Ahsa 31982, Saudi Arabia; graza@kfu.edu.sa

<sup>5</sup> Department of Mechanical Engineering, Faculty of technology, University of El Oued, P.O. Box 789, El Oued 39000, Algeria; nousseiba\_allag@yahoo.fr

<sup>6</sup> School of Natural Sciences, National University of Sciences & Technology, Islamabad 44000, Pakistan; shehla.mushtaq@sns.nust.edu.pk

\* Correspondence: wmir@kfu.edu.sa

**Abstract:** An ultrasound-assisted probe sonication route effectively prepared pure CuO and two-dimensional CuO–ZnO nanocomposites (NCs) for different ratios of CuO and ZnO, and the experimental and theoretical methods investigated the structural, photocatalytic, and electrochemical properties. The XRD (X-ray diffraction) patterns revealed a crystallite size (D) range of 25 to 31 nm for pure CuO and CuO–ZnO NCs. According to calculations, the sample's optical energy bandgap value (Eg) for the NCs is between 1.72 and 2.15 eV. Under UV light irradiation, the photocatalytic discoloration of pure CuO and CuO–ZnO NCs on fast blue (FB) dye was assessed. Under the influence of UV light, the CuO with 10% ZnO composite degrades 83.4% of the dye, which is greater than pure CuO and other NCs. The electrochemical properties of the prepared NCs materials have been studied using cyclic voltammetry and electrochemical impedance spectroscopy (EIS). The specific capacitance values were found to be 248 Fg<sup>−1</sup>, 301 Fg<sup>−1</sup>, 352 Fg<sup>−1</sup>, and 277 Fg<sup>−1</sup> for CuO, CuO + 5% ZnO, CuO + 10% ZnO, and CuO + 15% ZnO, respectively, at 1 A/g current density. Galvanostatic charge–discharge tests for these designed NCs show excellent capacitance performance in supercapacitors applications. These innovative results could be considered for expanding novel resources to scale for dual applications in photocatalysis and supercapacitors.

**Keywords:** probe sonication; CuO–ZnO nanocomposites; dye discoloration; supercapacitor



**Citation:** BaQais, A.; Alam, M.W.; Farhan, M.; Muteeb, G.; Allag, N.; Mushtaq, S. Probe-Sonicated Synthesis of CuO–ZnO Hybrid Nanocomposite for Photocatalytic and Supercapacitor Applications. *Inorganics* **2023**, *11*, 370. <https://doi.org/10.3390/inorganics11090370>

Academic Editor: Zemin Zhang

Received: 18 August 2023

Revised: 12 September 2023

Accepted: 14 September 2023

Published: 16 September 2023



**Copyright:** © 2023 by the authors. Licensee MDPI, Basel, Switzerland. This article is an open access article distributed under the terms and conditions of the Creative Commons Attribution (CC BY) license (<https://creativecommons.org/licenses/by/4.0/>).

## 1. Introduction

It is urgently necessary to accelerate the development of high-performance, low-cost, environmentally friendly renewable energy storage and conversion technologies [1–3] to meet the world's fast-rising energy demands.

Devices that store energy include ultracapacitors and supercapacitors, which are electrochemical capacitors. They have received more attention in recent years [4–8] because of their distinguishing qualities like higher power density and longer cyclic life than conventional batteries, as they are higher energy density capacitors, high-rate capacity, rapid charge–discharge mechanism, and eco-friendly. The most important upcoming energy storage technology is probably supercapacitors [9]. Due to their numerous uses in

industries such as load cranes, forklifts, electric cars, electric utilities, and factory power backups, supercapacitors have gained greater attention [10].

Electric double-layer capacitors (EDLCs) and pseudo-capacitors are the two categories of supercapacitors that are used to categorize them based on their charge storage mechanisms and electrode material types. Ion adsorption at the electrode–electrolyte interface allows for the electrostatic storage of charges in EDLCs. Activated carbon (AC), carbon aerogels, carbon nanotubes, and graphene are employed as carbon-based electrode materials [11,12]. Transition metal oxides, such as CuO, Cu<sub>2</sub>O, RuO<sub>2</sub>, MnO, NiO, and CoO, are employed in pseudo-capacitors to store charges due to electrochemical redox reactions [13–15] or conducting polymer electrode materials, such as polypyrrole, PANI, are used [16,17]. Hybrid supercapacitors combine the advantages of EDLCs and pseudo-capacitors, especially their high energy and power densities.

The unusual magnetic, catalytic, and electrical capabilities of metal oxide nanoparticles have attracted the greatest attention [18]. RuO<sub>2</sub> has become one of the transition metal oxides with the most promising candidates. RuO<sub>2</sub>'s utilization is nevertheless constrained by its increased cost and toxicity [19]. Therefore, it is crucial to create an environmentally sound substitute.

The metal oxide copper oxide (CuO), which has excellent redox properties, is employed in various applications. CuO is being studied due to its special qualities, like superior catalytic activity, ease of synthesis, eco-friendly, variety in nanoscale morphologies, abundance in nature, affordability, low toxicity, and favourable electrochemical properties [20–22]. CuO has been used in electrochemical processes as an electrode material for lithium-ion batteries, supercapacitors, solar systems, heterogeneous catalysts, and selected gas sensors [23]. Due to its enhanced electrochemical properties, it has been chosen as one of the materials of a nanocomposite electrode system. In the current work, we have doped CuO with various amounts of ZnO to enhance the catalytic characteristics of CuO nanoparticles.

Enhanced chemical, mechanical, and physical properties, a lower melting point, high diffusion, structural stability, an increased surface area, and high surface energy are all characteristics of CuO and ZnO in general [24]. CuO is usually used in combination with large-bandgap semiconductors, such as ZnO and TiO<sub>2</sub>, in order to improve their photocatalytic activity under solar light irradiation [25]. When coupled, an n-type semiconductor like ZnO with a broad bandgap energy of 3.37 eV and a p-type semiconductor like CuO with a narrow bandgap energy of 2.5 eV result [26].

Numerous synthesis techniques, ranging from simple thermal oxidation [27], electrochemical [28], precipitation [29], and hydrolysis [30], to highly complex techniques like so-gel [31], micro-emulsion system [32], Solvothermal method [33,34], and the microwave hydrothermal method [35,36], have been developed in response to the need for high purity CuO for industrial applications. These techniques are designed to change the nanomaterials' composition, particle size, crystalline structure, form, and functional stability to affect various aspects of the synthesized nanomaterial [37]. The characteristics of nanomaterials can be changed by altering the starting material concentration and doping agents employed in a particular synthesis technique. In the current work, we described the sonochemical production of CuO nanoparticles. Due to its reaction control circumstances, homogenous mixing, and management of the particle size distribution while being exposed to ultrasound, this preparation process has established with individual attention [38].

ZnO was doped into CuO NPs at various concentrations to create composite materials for photocatalytic and supercapacitor applications. The modified CuO-ZnO NCs electrode is put to the test as a supercapacitor electrode, and each composite's photocatalytic activity was assessed by measuring how quickly direct green and rapid blue degraded when exposed to UV light [39]. We believe these innovative results are significant because they may promote the efficient fabrication of these and other similar metal oxide semiconductors and provide us with vital information for advancing our understanding of photocatalytic activity.

Dyes are the most commonly used types of organic materials in various applications, including cosmetic, textile, ink, and leather industries, taking ~60–70% of dye production worldwide. It is reported that introducing dyes into the water resources causes serious threats to drinking water, aquatic life, and marine areas. In this regard, some significant examples are the mutagenicity and carcinogenicity of azo dyes and their derivatives [40]. Therefore, removing dyes from effluents has been extensively studied for many years. Although eliminating residual colors and organic dyes is a near-to-impossible task, many attempts have been made to clean up effluents impregnated with such harmful chemicals. Until now, a wide variety of physical/chemical techniques, such as photocatalysis, adsorption, etc., have been examined. Adsorption has been frequently considered a highly efficient approach to reducing contamination because of its simplicity, acceptable efficacy, and neutrality toward chemicals existing in wastewater [41]. Application of this technique in dye removal goes back to the early 20th century when dye molecules needed to be removed one by one due to their hazardous impacts on water resources. The broad bandgap (3.2 eV) semiconductor ZnO nanoparticle has a high exciton binding energy (60 meV) at room temperature. Additionally, the presence of UV photon energy causes electrons to be stimulated from the valence band (VB) to the conduction band (CB), which restricts the technology's potential use in applications for cleaning up pollutants. Therefore, it is crucial to design and adjust the ZnO crystal structure and morphology and reduce the electron–hole (e/h<sup>+</sup>) pair recombination rate using an appropriate dopant or additive for feasible photo discoloration under visible light. The most appealing method for improving the photocatalytic reactions and lowering the electron–hole pair recombination is the combination of two semiconductive materials. Among the different narrow bandgap metal oxide semiconductor nanomaterials investigated, a narrow bandgap (1.3 eV) monoclinic CuO was suitable to improve the photocatalytic performance of ZnO. This is due to CuO's increasing use in gas sensing, rechargeable lithium-ion batteries, supercapacitors, solar hydrogen processing, catalytic processes, and photovoltaic applications. The energy gaps of ZnO (3.2 eV) and CuO (1.3 eV) encompass the ultraviolet and visible spectra, which confirms their effective candidacy for the catalytic discoloration of dyes. They are also produced in an environmentally benign manner and are easily accessible [42]. Table 1 shows the synthesis methods of CuO-ZnO nanocomposites and their applications in previous studies.

**Table 1.** Synthesis methods of CuO-ZnO nanocomposites and their applications.

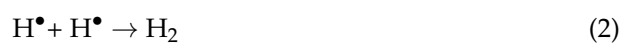
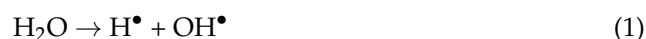
Sl. No	Synthesis Method	Work Done	Reference
1	Solution combustion	Photoluminescence and catalytic 4-nitrophenol reduction	[43]
2	Solid-state preparation of CuO/ZnO	Functional supercapacitor electrodes and photocatalysts	[44]
3	Nanocomposites co-precipitation method	Photocatalytic and supercapacitors	[45]
4	Chemical vapor deposition	Acetone sensor	[46]
5	Hydrothermal synthesis	H <sub>2</sub> S gas sensor	[47]
6	Green synthesis	Photocatalytic and Sensor Applications	[48]
7	Hydrothermal method	Photo discoloration of methyl orange dye and antifungal study	[49]
8	Sol-gel process	Glucose sensing	[50]
9	Vapor transport method	Photo discoloration of resazurin (Rz) dye	[51]
10	Sol-gel method	Photo discoloration of methyl orange dye	[52]

## 2. Materials and Methods

### 2.1. Synthesis of the CuO–ZnO Hybrid Nanocomposite

The CuO–ZnO hybrid NCs were obtained from the sulphate precursors like CuSO<sub>4</sub>·5H<sub>2</sub>O (99% Sigma Aldrich St. Louis, MO, USA) (0.25 M) and ZnSO<sub>4</sub>·7H<sub>2</sub>O (99%, Sigma Aldrich) (5, 10, and 15 M) under ultrasound irradiation. By adding 0.5 M NaOH (99%, Sigma Aldrich St. Louis, MO, USA), the pH of the solution above was adjusted to 12. Using a probe sonicator (Model PRO-500, 20 kHz, 500 W STERICOX INDIA PRIVATE LIMITED Delhi, India), the reaction mixture in the sonication flask was ultrasonically treated for 30 min. The probe has a diameter of 13 mm, is composed of high-grade titanium, and operates at a frequency of 40 kHz with 20 percent amplitude. After 30 min of sonication, the final product obtained was filtered using Whatman filter paper and washed with distilled water and absolute ethanol (99%, Sigma Aldrich). In the preheated furnace, the filtered residue was dried for 6 h using an oven and calcinated at 500 ± 10 °C for 3 h.

Ultrasonic waves cause bubble formation in a solvent. These bubbles, on explosion, release a huge amount of energy capable of breaking the molecular bonds between precursor particles and finally producing finer particles [53,54]. The energy released during the explosion of the bubbles can also result in the breakage of covalent bonds among atoms in the solvent generating free radical species. Free radicals produced are extremely reactive and can reveal a product's formation. Under ultrasonic waves, the solvent water generates •H and •OH radicals that are highly reactive, which on further reaction, produce H<sub>2</sub> and H<sub>2</sub>O<sub>2</sub> as presented in Equations (1)–(3):



The H<sub>2</sub> and H<sub>2</sub>O<sub>2</sub> can influence oxidation–reduction reactions [55,56] and oxidize sulphates, copper, and zinc into their respective oxides, CuO and ZnO, which recombine to form the end product.

### 2.2. Preparation of Working Electrodes

The electrodes were created by 45 min of grinding in an agate mortar, a mixture of 70% sample (0.35 g), 15% graphite powder (<20 µm, Sigma Aldrich), and 15% PTFE solution (60 weight % dispersion in water) as a binder to form a uniformly thin sheet layer. This layer was then adhered to nickel mesh and pressed at 20 MPa to provide high-quality electrical contact with the nickel mesh and the active material (2 cm × 1 cm). To ensure the electrode made contact with the electrolyte, it was dipped in a 1.0 M KOH solution for around 30 min, and Teflon tape was used to insulate the electrode.

### 2.3. Electrochemical Measurements

A fabrication of a supercapacitor cell is powered by a specific blend of CuO and CuO–ZnO composite electrodes with 1M potassium hydroxide (KOH). An indicator (platinum), reference (Ag/AgCl), and working electrode were used for electrochemical measurements. The CHI608E (CH Instrument) conducts impedance spectroscopy, cyclic voltammetry, and galvanostatic charge–discharge methods. The following Equation (4) [57] was used to determine the total capacitance “C” of the electrodes through a.c impedance spectroscopy (frequency range: 10 mHz–10 kHz):

$$C = -1/Z''\omega \quad (4)$$

where Z'' is the imaginary part of the complex impedance and ω is the angular frequency.



The capacitance values from cyclic voltammetry were calculated using the following mathematical relation [58]:

$$C_{sp} = \frac{\int IdV}{S \cdot \Delta V \cdot m} \quad (5)$$

$$C = i \cdot \Delta t / m \Delta V \quad (6)$$

where,  $\int IdV$  specifies the integral area of one complete cycle of CV curve,  $\Delta V$  is the potential window (V), 'm' is the mass of the active material (mg),  $S$  is the scan rate ( $\text{mV s}^{-1}$ ),  $I$  (A) is the discharge current density, and  $\Delta t$  (s) is the discharge time.

#### 2.4. Characterizations

Philips X'pert-PRO X-ray diffractometer with graphite monochromatized Cu K $\alpha$  ( $\lambda = 1.5418 \text{ \AA}$ ) radiation was used to obtain the PXRD patterns with a scan rate of  $2 \text{ min}^{-1}$  and  $2\theta$  ranging from  $10^\circ$  to  $80^\circ$ . For cyclic voltammetric tests, the measurement was performed on a CHI604E potentiostat with a tri-electrode system, consisting of a working electrode, platinum wire, and Ag/AgCl as the working, counter, and reference electrodes, respectively, and the electrolyte being a 1.0 M KOH solution. The potential range was  $-1.0 \text{ V}$  to  $0.6 \text{ V}$  (vs. Ag/AgCl electrode) and the scanning rate was  $5 \text{ mV/s}$ ,  $10 \text{ mV/s}$ ,  $15 \text{ mV/s}$ ,  $20 \text{ mV/s}$ , and  $25 \text{ mV/s}$ , for the Galvanostatic charge–discharge measured at a current density of  $5 \text{ Ag}^{-1}$  within the potential window of  $0$  to  $0.6 \text{ V}$  vs. Ag/AgCl. In addition, with an AC amplitude of  $5 \text{ mV}$  and a frequency range of  $1 \text{ Hz}$  to  $1 \text{ MHz}$ , EIS measurements were also carried out here.

### 3. Results and Discussion

#### 3.1. PXRD Analysis

The pure CuO and ZnO-doped CuO blended NCs with varied compositions are revealed in Figure 1a's PXRD pattern. The recorded XRD peaks of CuO (110), (002), (111), (202), (020), (113), (311), and (004) are complied with the reference pattern of the monoclinic structure (JCPDS 05–0661) [59]. Based on the information in the JCPDS 36–1451 file [60], the hexagonal wurtzite structure was identified as the crystal phase of the synthesized ZnO particles. As seen in Figure 1, the (100), (110), (002), (101), (111), (102), (202), (020), (110), (113), (103), (200), (112), (311), and (004) planes all exhibit the hexagonal wurtzite structure. For pure ZnO, the planes are (100), (002), (101), (102), (103), (110), (200), (112), and (201), respectively. Experimental diffraction peaks for both samples are clearly defined, demonstrating the high quality and crystallinity of the powders [33,34]. The crystallite size ( $D$ ) is estimated using eq for CuO–ZnO hybrid NC. 7 (Scherrer's formula).  $D$  is observed between 25 and 30 nm.

$$D = \frac{K\lambda}{\beta \cos \theta} \quad (7)$$

wherein, 'K'—constant, ' $\lambda$ '—wavelength, and ' $\beta$ '—full width at half maximum (FWHM).

The crystallite size ( $D$ ) for the CuO–ZnO hybrid nanocomposite was calculated from the prominent peaks (101) and (111) and was evaluated to be in the range of 25–31 nm. The straining that happened in the  $\text{Cu}^{2+}$  sites of the CuO host lattice due to  $\text{Zn}^{2+}$  inclusion caused the increase in crystallite size observed. The rise in crystallite size may be attributed to the small variation in ionic radii of  $\text{Cu}^{2+}$  (0.073 nm) and  $\text{Zn}^{2+}$  (0.074 nm) [61,62]. Additionally, a slight shift of the main diffraction peak (111) towards a lower ( $2\theta$ ) angle can be observed with an increment in ZnO concentration, which could be due to the exchange of  $\text{Cu}^{2+}$  ions of the CuO host lattice structure by  $\text{Zn}^{2+}$  ions. The exchange of  $\text{Cu}^{2+}$  ions by  $\text{Zn}^{2+}$  can be established by studying the lattice parameters from the Equation (8) [63]:

$$\frac{1}{d_{hkl}^2} = \frac{4}{3} \left( \frac{h^2 + hk + k^2}{a^2} \right) + \frac{l^2}{c^2} \quad (8)$$

wherein;  $d_{hkl}$ —interplanar distance,  $h, k, l$ —Miller indices;  $a, b$ , and  $c$ —lattice parameters.

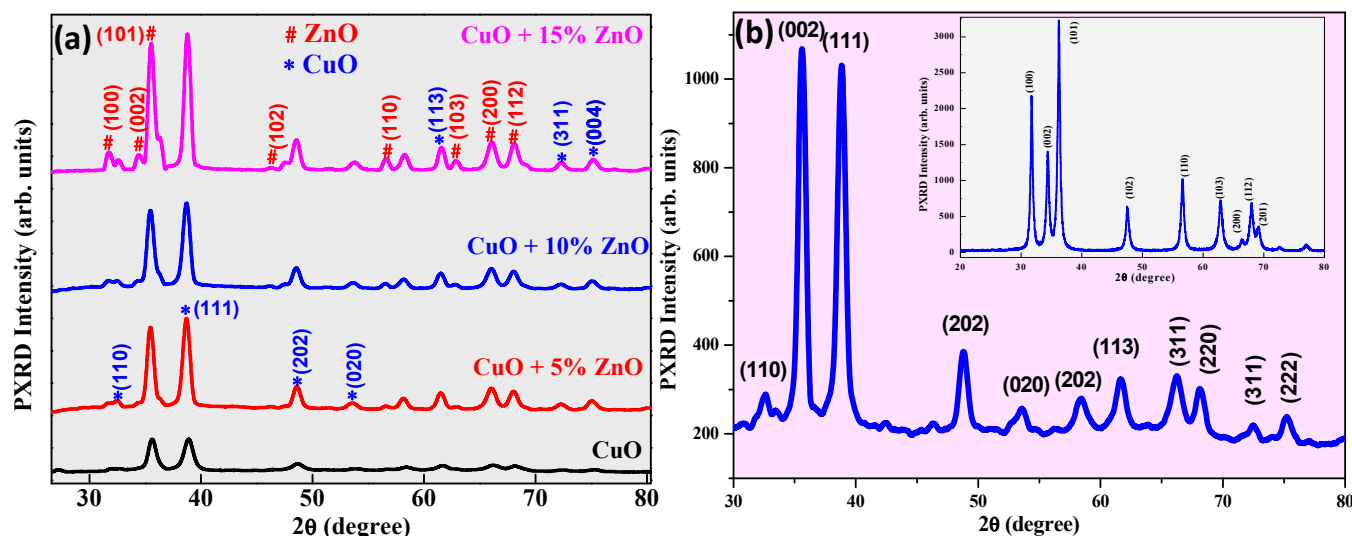


**Figure 1.** PXRD spectra of (a) CuO–ZnO hybrid nanocomposites (b) Non-calcined CuO NPs and pure ZnO NPs (inset).

All samples displayed lower lattice parameters (*c*) values accredited to the exchange of Cu<sup>2+</sup> by Zn<sup>2+</sup> ions of different ionic radii [64,65]. The slight shift in the peak towards the side of the lower (2θ) angle and variations in the values of d-spacing and lattice parameters confirm the doping of ZnO into the CuO lattice structure. Figure 1b shows the XRD pattern of the non-calcinated CuO sample, which proves CuO particles were formed under ultrasonic waves. The inset of Figure 1b shows the XRD pattern of the ultra-sonicated ZnO sample. Table 2 shows the physical and optical properties of CuO-ZnO hybrid NCs.

**Table 2.** Physical and optical properties of CuO-ZnO hybrid NCs.

ZnO Doping Concentration (%)	Crystal Size (nm)	d-Spacing (Å°)	Lattice Parameters (nm)		The Band Gap (eV)	Unit Cell Volume
			a = b	c		
0	25	1.33	2.30	1.36	1.72	81.08A <sup>3</sup>
5	28	1.76	3.06	0.57	1.78	78.25A <sup>3</sup>
10	28	1.76	3.06	0.57	1.85	76.12A <sup>3</sup>
15	31	1.47	2.55	1.80	2.15	73.08A <sup>3</sup>

### 3.2. Morphological and EDAX Analyses

SEM pictures in Figure 2a–d show the morphology of synthesized CuO and CuO-ZnO hybrid NCs with different compositions of zinc oxide (0%, 5%, 10%, and 15%). The samples show agglomeration with a diameter of approximately  $\sim 10\text{ }\mu\text{m}$ . The amount of agglomeration grew with an increase in ZnO concentration, as shown from the micrographs in Figure 2a,b, and Figure 2c,d displays decorating of ZnO onto CuO nanoparticles.

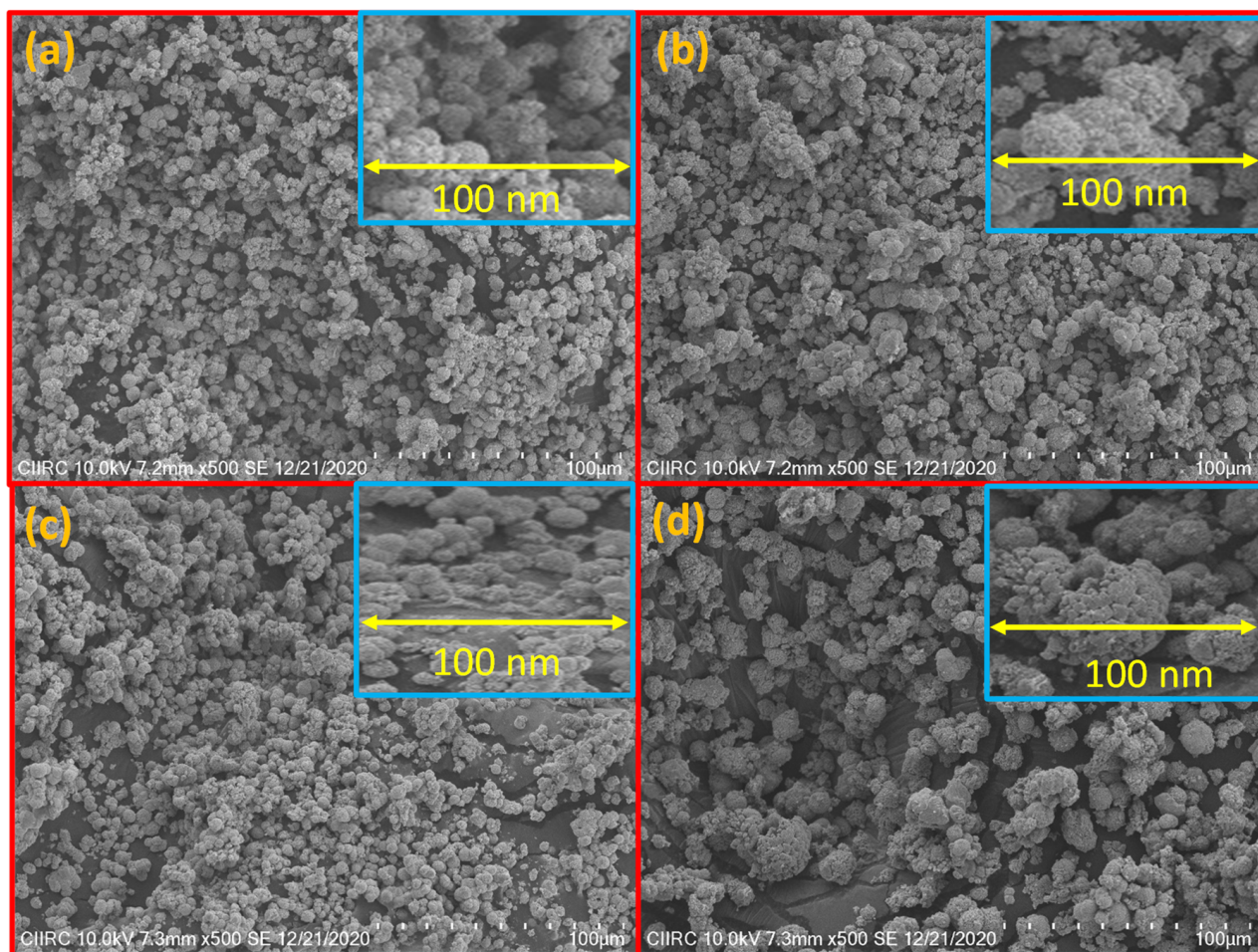


**Figure 2.** SEM micrographs of (a) CuO, (b) CuO + 5% ZnO, (c) CuO + 10% ZnO, and (d) CuO + 15% ZnO.

The sample was comprised of Cu, Zn, and O elements with different weight percentages as shown in Figure 3a–d. The EDX spectrum of the CuO (Figure 3a) displayed peaks for Cu and O which confirms the formation of the CuO metal oxide. From Figure 3b–d, it is evident that Zn is doped onto CuO. Figure 4 shows the DRS and energy bandgap spectra of the samples.

The Kubelka–Munk equation  $F(R)$ , widely used to transform diffused reflectance into an equivalent absorption coefficient and utilized to examine particles (Figure 4a), is provided by Equation (9) [66]:

$$F(R) = \frac{(1 - R)^2}{2R} \quad (9)$$

where  $R$ —reflectance,  $F(R)$ —Kubelka–Munk function.

Equation (10) was used to compute the optical energy gap using the Tauc relation:

$$F(R) h\nu = A (h\nu - E_g)^n \quad (10)$$

where  $n = 1/2$  and 2 is direct and indirect transitions.

The optical energy gap was calculated using the Tauc relation as in Equation (10) thereby giving a direct band. The plots of  $(F(R))^2$  vs.  $h\nu$  synthesized hybrid NCs were displayed in Figure 4b. The samples and their optical energy gap  $E_g$  values of CuO, CuO + 5% ZnO, CuO + 10% ZnO, and CuO + 15% ZnO were 1.72, 2.38, 1.85, and 2.21 eV, respectively (inset Figure 4b). The deduced bandgap energy value of CuO was ~1.72 eV, which was found to be somewhat higher compared to the previously documented value of

1.83–2.08 eV [55,56]. The method of synthesis used in the current work can be implicated in the variation in bandgap values. An increase in the energy bandgap from 1.72 eV to 2.15 eV was seen simply by increasing the ZnO concentration.

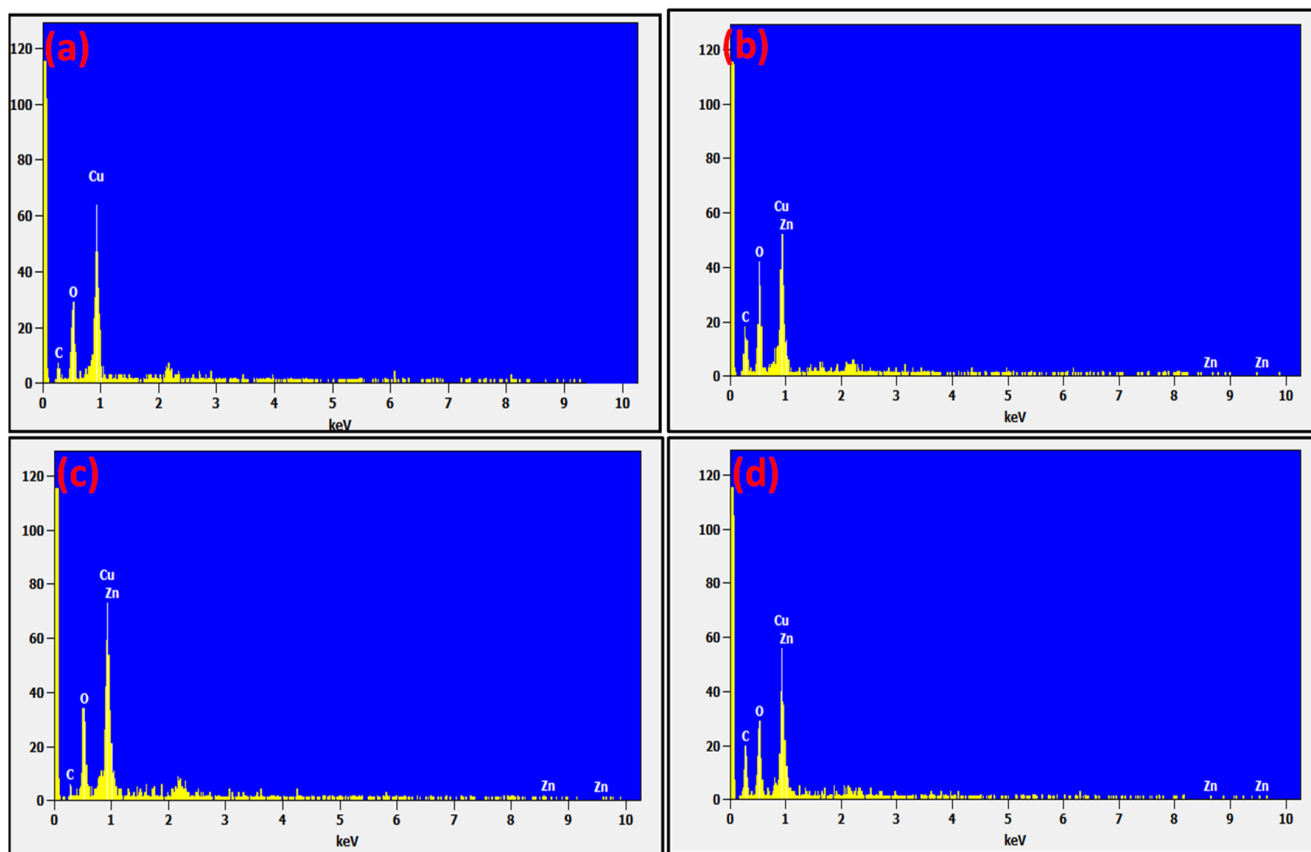


**Figure 3.** EDAX spectra of (a) CuO, (b) CuO + 5% ZnO, (c) CuO + 10% ZnO, and (d) CuO + 15% ZnO.

This hypochromic movement can be due to the familiar Burstein–Moss effect [57]. Semiconductors with n-type doping generally exhibit this effect. The fermi level rises during n-type doping in semiconductors as electrons fill the lower level of the conduction band. This causes a shift towards shorter wavelengths in the band edge absorption. As a result, a photon with a shorter wavelength than that of the undoped semiconductor is released when photo-excited electrons and positive holes recombine.

### 3.2.1. Thermogravimetric Analysis (TGA) and Differential Thermal Analysis (DTA) Analysis

TGA and DTA analyses were used to examine the thermal characteristics of CuO and CuO-ZnO hybrid NCs in their as-prepared state (Figure 5a–d). Due to the loss of free and coordinated water molecules in the samples, the first weight loss of around 30% in the TGA curve up to 300 °C was followed by an endothermic peak at 165 °C [67]. Due to the loss of capping agent (PEG) and glycerol, the TGA curve shows additional weight variations (20%) in the 210–600 °C temperature range. It should be emphasized that the TGA curve’s apparent weight increases beyond 580 °C due to an instrument artefact. Between 200–800 °C, there are no changes in the TGA curve, which suggests the development of stable CuO-composite materials.

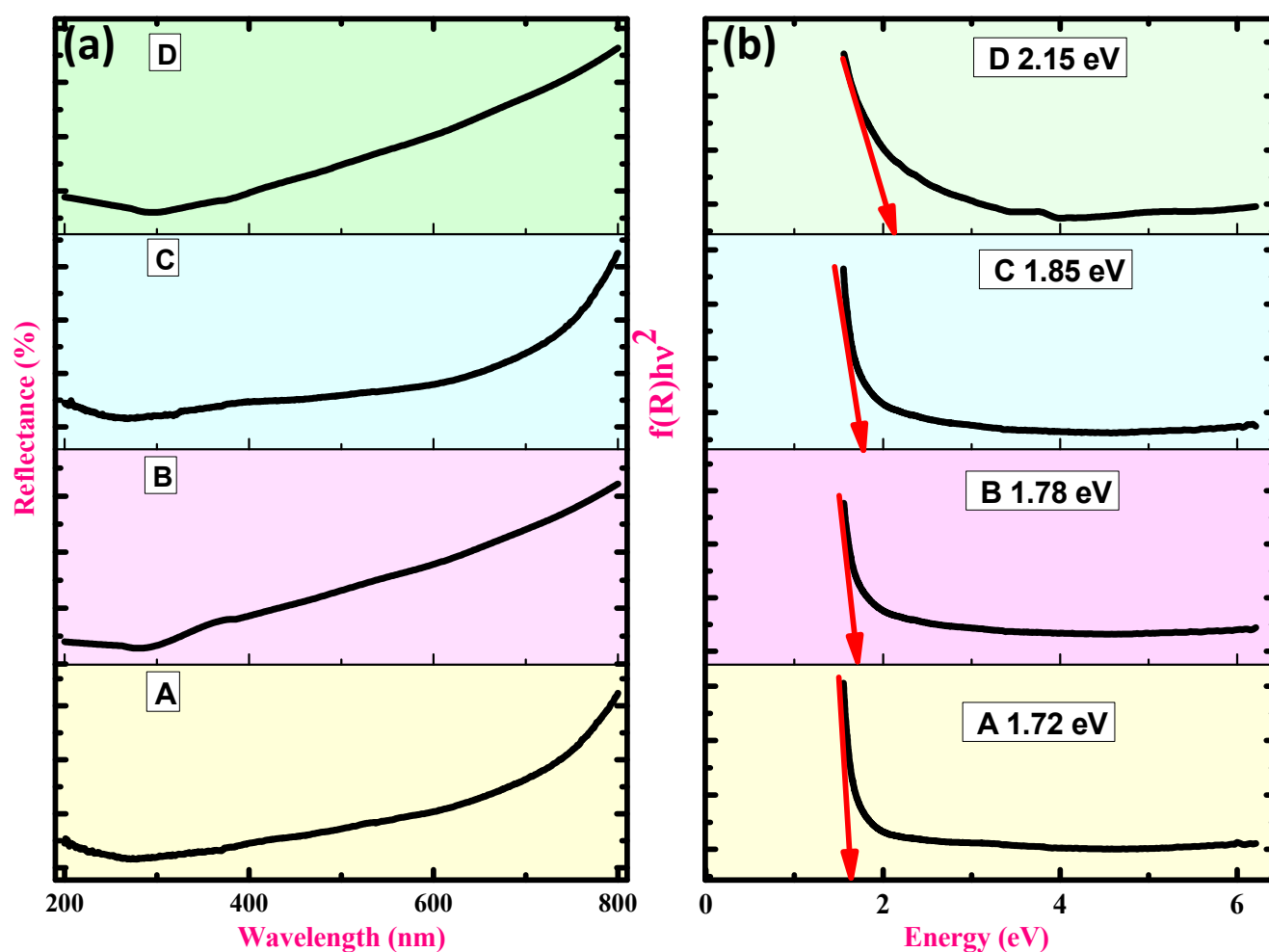
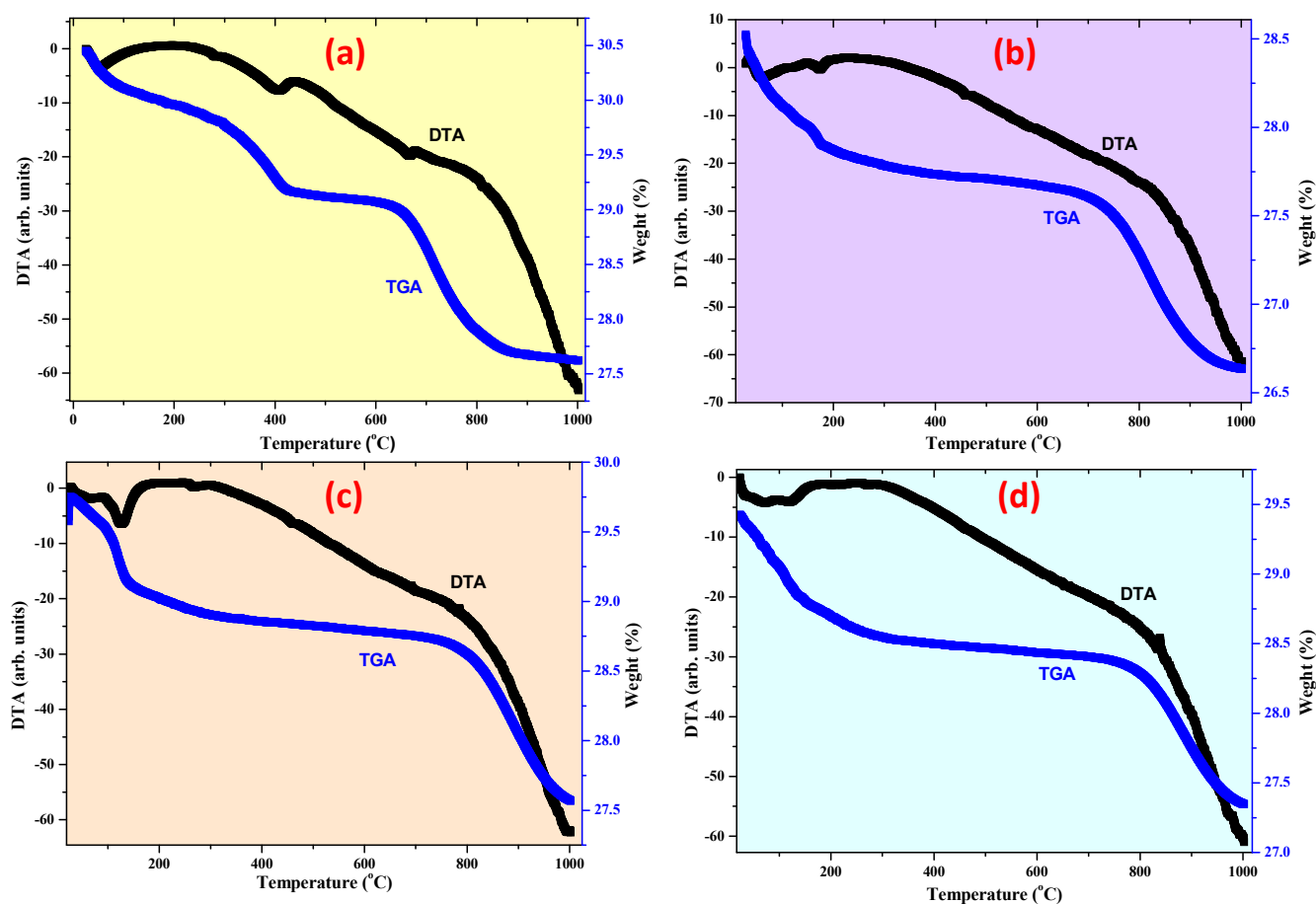


**Figure 4.** DRS and energy bandgap spectra of samples (a,b); (A) CuO, (B) CuO + 5% ZnO, (C) CuO + 10% ZnO, and (D) CuO + 15% ZnO.

### 3.2.2. Photocatalytic Studies

ZnO has potential as a photocatalyst material because of its property of wide bandgap. It has been reported that zinc oxide is an N-type semiconductor with a wide bandgap of 3.37 eV and a large exciton binding energy of 60 meV. Pure ZnO nanoparticles absorb around 355–392 nm while they emit around 392–524 nm which varies according to their intrinsic defects and size. The fast blue (FB) in an aqueous solution was broken down by the photocatalytic experiment of the CuO, CuO + 5% ZnO, CuO + 10% ZnO, and CuO + 15% ZnO photocatalysts under UV–visible light radiation. Photocatalytic experiments were performed in a circular glass reactor using a 125 W medium-pressure mercury vapor lamp as the UV light  $\geq 370$  nm wavelength source at room temperature. In each experiment, 100 mL of fast blue solution was combined with 0.1 g of the photocatalyst at a concentration of 15 mg L<sup>−1</sup>. There was a 23 cm gap between the light source and the sample to prevent heat from the light source. The reaction mixture was exposed to UV light in the open air for 120 min, and 5 mL of the sample solution was taken out and measured every 15 min in the 200–800 nm UV–visible range.





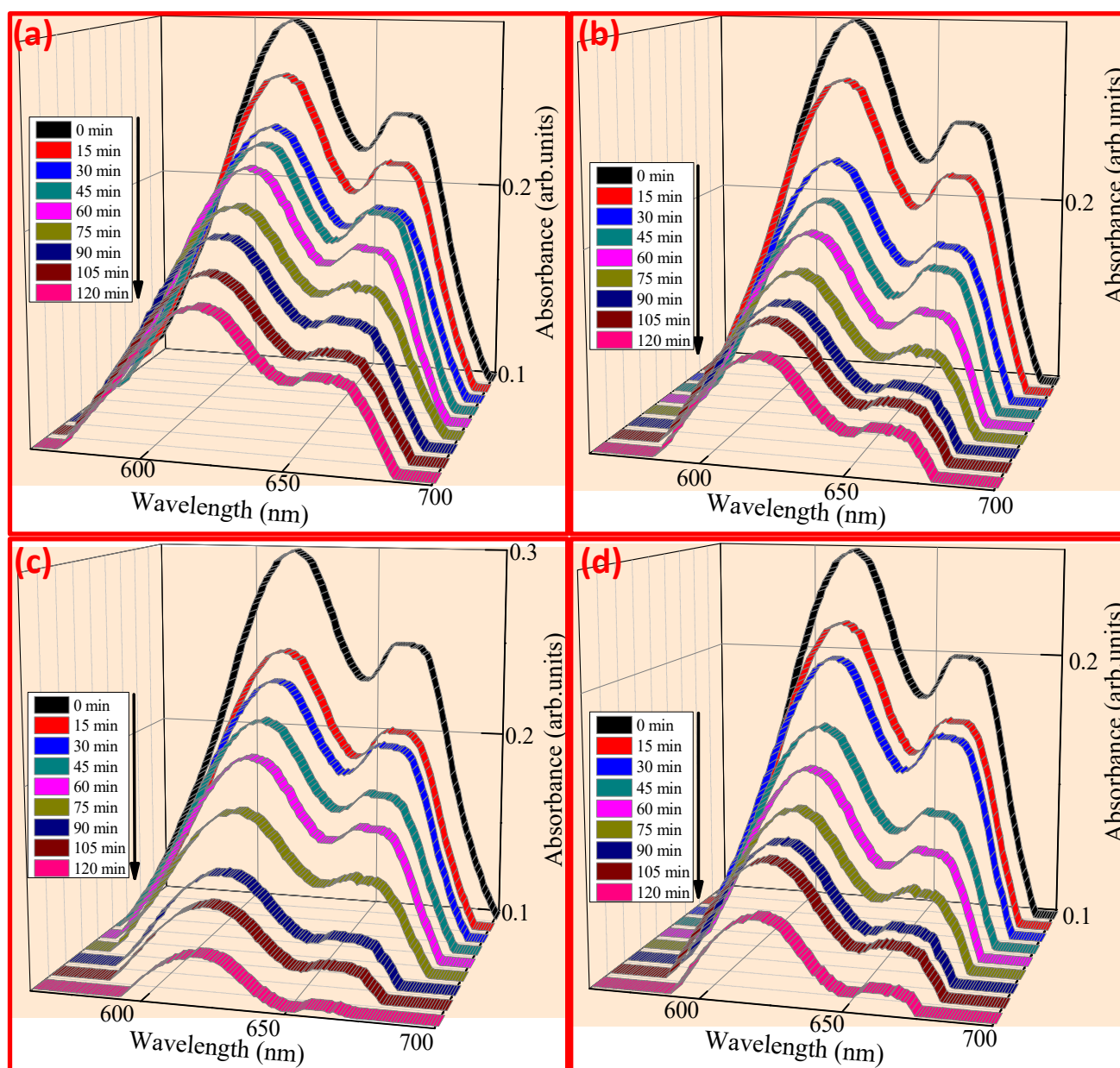
**Figure 5.** Thermal analysis (TGA-DTA) of samples (a) CuO, (b) CuO + 5% ZnO, (c) CuO + 10% ZnO, and (d) CuO + 15% ZnO.

Figure 6a–d shows the dye decomposition absorbance spectra with a maximum wavelength of 610, 613, 614, and 613 nm for CuO, CuO + 5% ZnO, CuO + 10% ZnO, and CuO + 15% ZnO. The discoloration of FB aqueous solution evaluated the photocatalytic activity of CuO NPs. As shown in Figure 7a,b, after 120 min of UV light, the photo discoloration rate of FB dye decolorized up to 58.75%, 66.5%, 83.4%, and 74.3% for CuO, CuO + 5% ZnO, CuO + 10% ZnO and CuO + 15% ZnO, respectively [68,69]. The discoloration percentage of the dyes was determined using Equation (11):

$$\% \text{discoloration} = \frac{C_o - C_e}{C_o} \times 100 \quad (11)$$

where  $C_o$ —initial dye concentration and  $C_e$ —dye concentration after adsorption at time  $t$  seconds. Further,  $C/C_o$  values were also calculated by the following Equation (12):

$$\log \frac{C}{C_o} = -Kt \quad (12)$$



**Figure 6.** Absorbance spectra of FB dye under UV light (a) CuO, (b) CuO + 5% ZnO, (c) CuO + 10% ZnO, and (d) CuO + 15% ZnO.

$C_0$  and  $C$ —dye concentrations at time  $t = 0$  min and at the time of testing, respectively, and  $k$ —first order rate constant. The determined data showed that  $\log C/C_0$  and  $k$  had a linear relationship, supporting first-order kinetics. For CuO, CuO + 5% ZnO, CuO + 10% ZnO, and CuO + 15% ZnO, the slope  $k$  was estimated for FB under UV light and was  $4.060 \times 10^{-3} \text{ min}^{-1}$ ,  $4.063 \times 10^{-3} \text{ min}^{-1}$ ,  $4.068 \times 10^{-3} \text{ min}^{-1}$ , and  $4.065 \times 10^{-3} \text{ min}^{-1}$ , respectively.

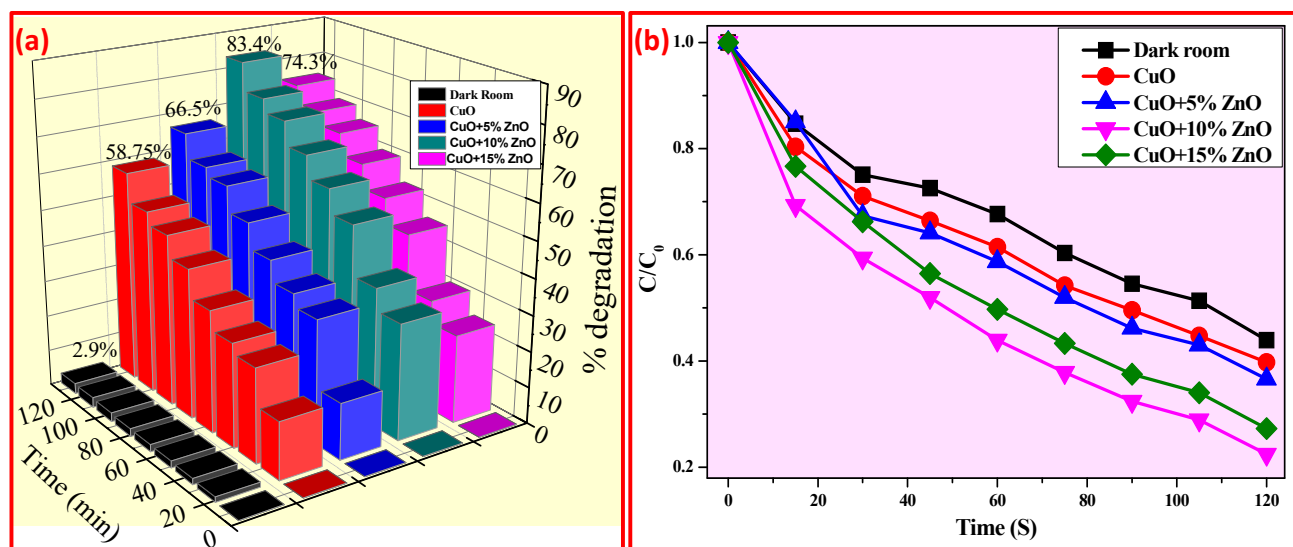


**Figure 7.** (a) % decolorization and (b) Plot of  $C/C_0$  vs. irradiation time of FB dyes under UV light (dark room, CuO, CuO + 5% ZnO, CuO + 10% ZnO, and CuO + 15% ZnO).

On UV light illumination, both photocatalysts (ZnO and CuO) were excited, resulting in the generation of electron–hole pairs. Since the valence band edge of ZnO is more positive than that of CuO, the holes may migrate from the VB of ZnO to the VB of CuO and react directly with organic contaminants. The conversion of  $\bullet\text{OH}$  from  $\text{H}_2\text{O}$  has a potential of +2.38, which is lower than ZnO VB potentials. Simultaneously, water may oxidize to a hydroxyl radical ( $\bullet\text{OH}$ ) while reacting with  $h^+$  at the (VB) of ZnO thereby improving the photocatalytic efficiency. As a result, many electrons are collected at the CB of ZnO because ZnO is more negative than CuO and tends to flow from the CB of ZnO to the CB of CuO [68]. Furthermore, the electrons in CB of ZnO and CuO may not react with the adsorbed  $\text{O}_2$  on the catalyst's surface to generate  $\text{O}_2^{\bullet-}$  because ZnO and CuO's CB energy levels are more positive than the standard potential of  $\text{O}_2/\text{O}_2^{\bullet-}$  (−0.33 eV). A series of reactions take place when  $\text{H}_2\text{O}$  and  $\text{O}_2$  are present. With the help of positive holes,  $\text{H}_2\text{O}$  is oxidized, and  $\text{O}_2$  is reduced with the help of the CB's photoelectron. Reactive  $\text{O}_2$  species are produced, including  $\text{H}_2\text{O}_2$ ,  $\text{O}_2^{\bullet-}$ , and  $\text{OH}^\bullet$  and holes may actively involve the decolorization of dye solution completely, as shown in Figure 8 [68–70].



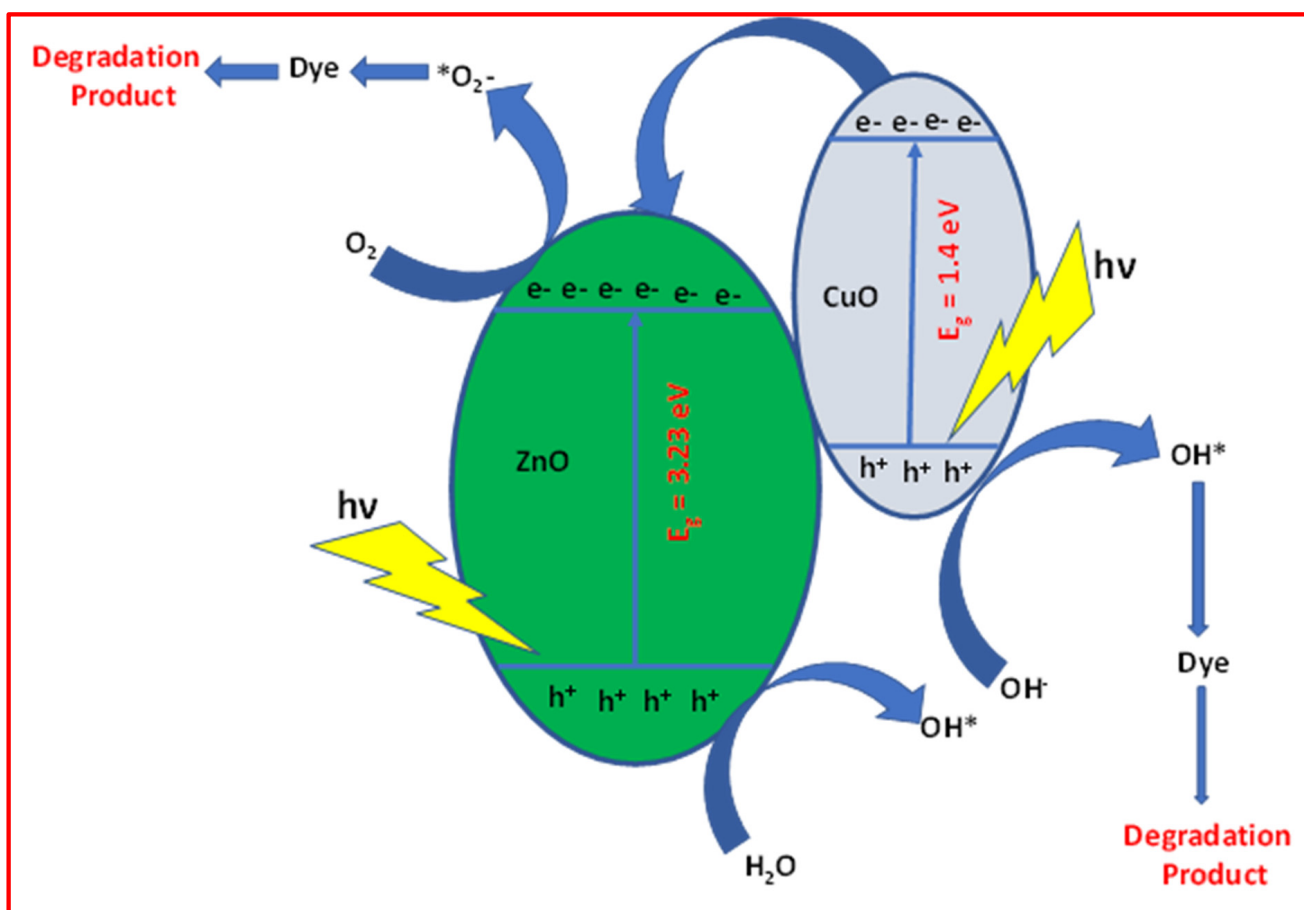
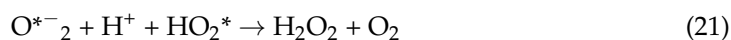


**Figure 8.** Mechanism for the photocatalytic discoloration of FB dye under UV light for CuO + 10% ZnO nanocomposite.

Consequently, the amount of CuO + 10% ZnO photocatalyst determines the dye's photo discoloration activity. Under UV light, the decolorization activity of FB dyes was investigated by varying the catalyst dose from 20 to 60 mg and maintaining the concentration (20 ppm) (Figure 9a). Over a 120 min period, a specific dose of catalyst (60 mg) improved the rate of dye photo discoloration. A further increase in the catalyst quantity to 60 mg reduced the activity due to the effects of screening and light scattering [71,72]. Consequently, experimental procedures with FB dye concentrations ranging from 10 to 25 ppm were used to determine the ideal dye concentration. As the concentration of CuO + 10% ZnO in the dye increases, less dye molecule adsorption occurs on the photocatalyst surface. Thus, the 20 ppm dye concentration exhibits better photo discoloration activities, as shown in Figure 9b [73–75].

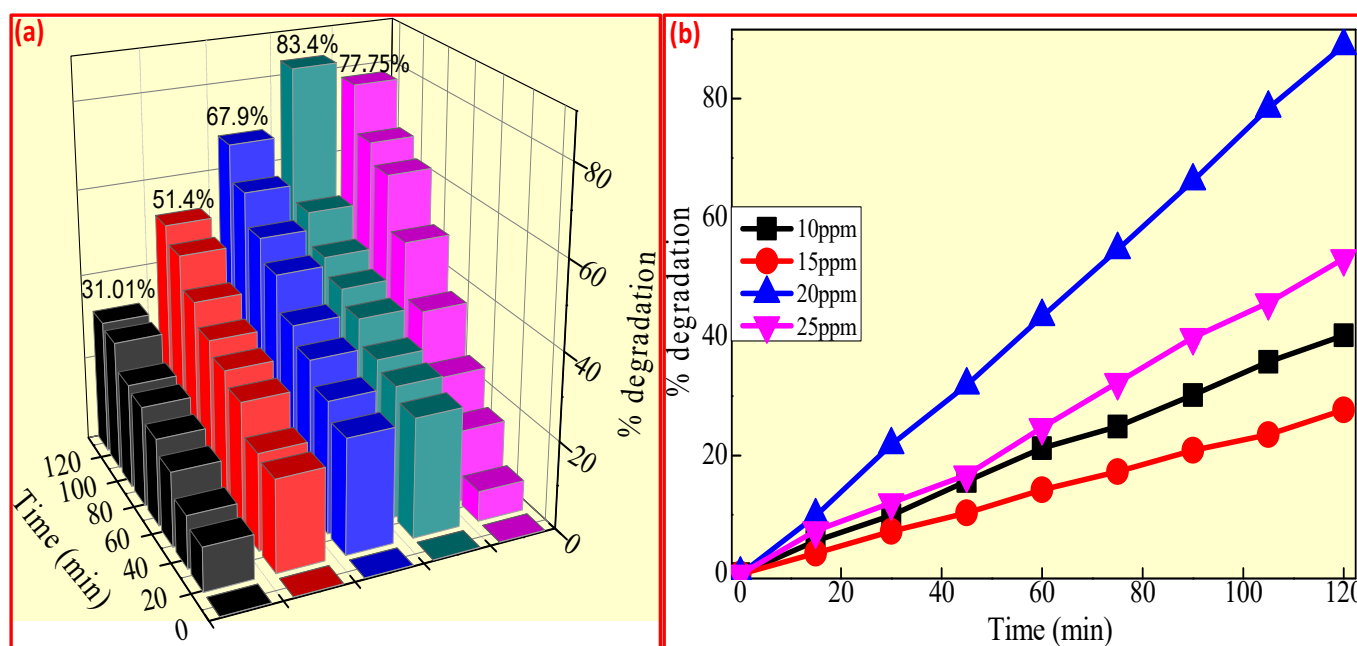


**Figure 9.** Rate of photo discoloration of FB under UV light (a) different dye concentrations and (b) different ppm of CuO + 10% ZnO.

The recyclability of the prepared catalysts is a significant consideration when determining the catalyst's practical application and scalability. The photocatalysts were separated by centrifugation without washing after each run for the recycling ability process, and the degraded FB supernatant was removed before adding fresh FB solution. Five recycling experiments were conducted to determine the CuO + 10% ZnO sample's durability and recyclability for photocatalytic discoloration Figure 10a. The CuO + 10% ZnO catalyst could demonstrate visible-light-induced photocatalytic activity in five subsequent cycling experiments without regeneration. The concentration of FB was shown to drop in each cycle. Despite this, some photocatalytic activity was lost after recycling. For the second through five runs, the activity in the first run was higher than that seen in these sequential uses at the end of a 2 h visible light irradiation. The catalyst maintained some activity, as seen by the final run's observation of a 10% discoloration of FB, even though it was speculated that the intermediates from the decomposed FB may have blocked the active sites [76–78]. In Figure 10b, it was found that, without scavengers, the photocatalytic discoloration of FOR on CuO + 10% ZnO was ~83.4% after 2 h. A total of 2 mg  $\text{AgNO}_3$  as a scavenger of  $\text{O}_2^{\cdot-}$  was added in the photocatalytic system causing the photo discoloration of FB on CuO + 10% ZnO to decrease significantly, reducing the discoloration to 28%. This revealed that  $\text{O}_2^{\cdot-}$  largely influenced the photocatalytic breakdown of FB over CuO + 10% ZnO. As a hole scavenger, 2 mg of ethanol was used. The FB was degraded by this addition by up to 34.26%, with little difference from the unquenched test. As a  $\cdot\text{OH}$  scavenger, 2 mg benzenic acid was introduced to the photo discoloration system, which caused a 41% FB discoloration [79–82]. According to the results of the quenching tests,  $\text{O}_2^{\cdot-}$  was the reason for the discoloration of FB by CuO + 10% ZnO under UV light, with  $\cdot\text{OH}$  and holes species being much less significant. Table 3 illustrates the comparison of photocatalytic activity of the CuO-ZnO nanocomposites with recent reports. In the present study, the modified CuO-ZnO NCs exhibited good photocatalytic activity as measured by the rate of discoloration of direct green and rapid blue when exposed to UV radiation.



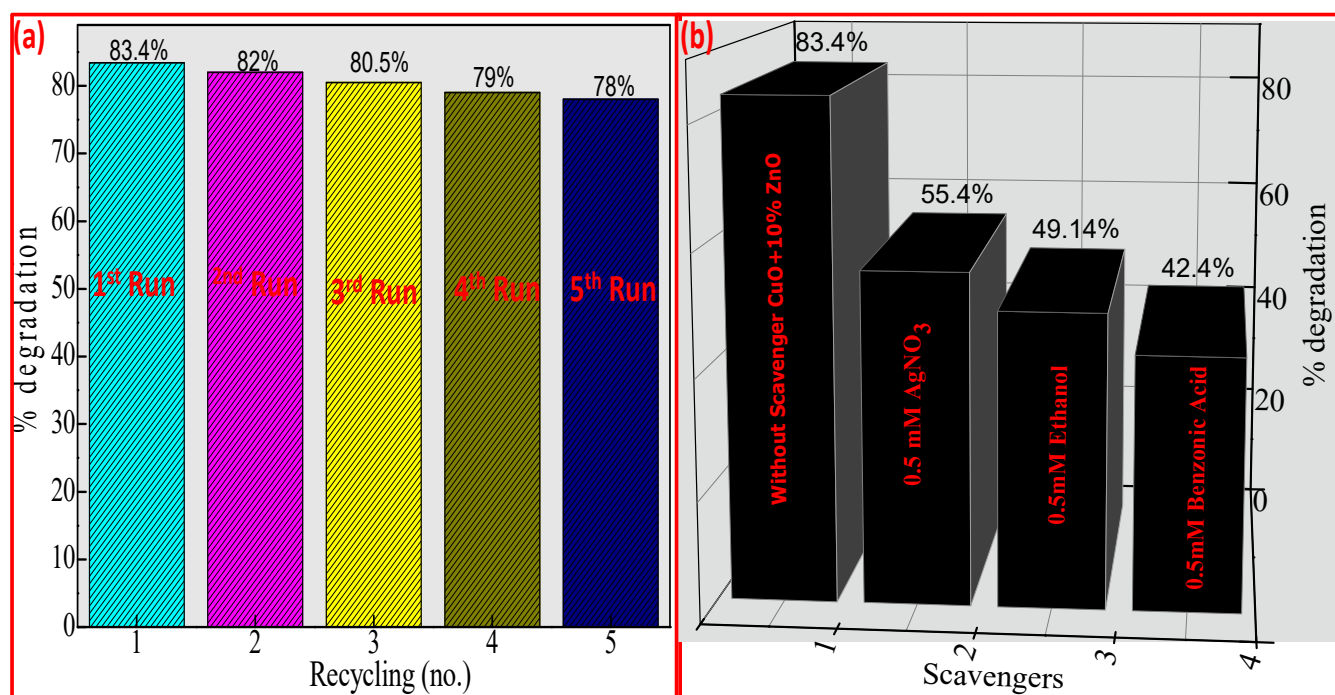


**Figure 10.** (a) Recyclability and (b) Scavenging examinations of FB under UV light of CuO + 10% ZnO.

**Table 3.** Comparison of photocatalytic performance of CuO-ZnO nanocomposites with recent reports.

S. No	Material	Pollutant	Irradiation Source	Discoloration Efficiency (%)	References
1	CuO-ZnO	Methylene blue	Halogen lamp	82	[83]
2	ZnO/CuO/SnO <sub>2</sub>	Fast green	Visible light	93.68	[84]
3	Chitosan/CuO-ZnO	Rapid green	Solar lightUV light	60.2391.21	[85]
4	Silane-TiO <sub>2</sub>	Methylene blue	UV light	82	[86]
5	CuO-ZnO	Rapid blue	UV light	83.4	Present work

Cyclic voltammetry (CV) to determine the capacitive performance and electrochemical properties of supercapacitor electrodes is a helpful approach for CuO, CuO-ZnO, CuO + 10% ZnO, and CuO + 15% ZnO (Figure 11). Three combinations of electrode systems allow for the performance of CV analysis (−0.6 V to +1.0 V (vs. Ag/AgCl)). Figure 11a–d depicts the behavior of CuO and CuO-ZnO composites in 1 M KOH as an electrolyte at various scan speeds (10, 20, 30, 40, and 50 mV/s) [87]. Good electrode stability is demonstrated by the electrodes' anodic and cathodic peak positions not significantly changing with the growth cycles [88].

Figure 12 shows a sequence of a cyclic voltammogram (at a scanning rate of 10 mVs<sup>−1</sup>) of CuO, CuO + 5% ZnO, CuO + 10% ZnO, and CuO + 15% ZnO electrodes for 25 cycles, respectively. It can be observed that the locations of anodic and cathodic peaks of both electrodes did not nearly vary with growing cycles. Thus, it can be supposed that the electrodes have a stable cycle and considerable structural modifications did not take place while charging and discharging [89].

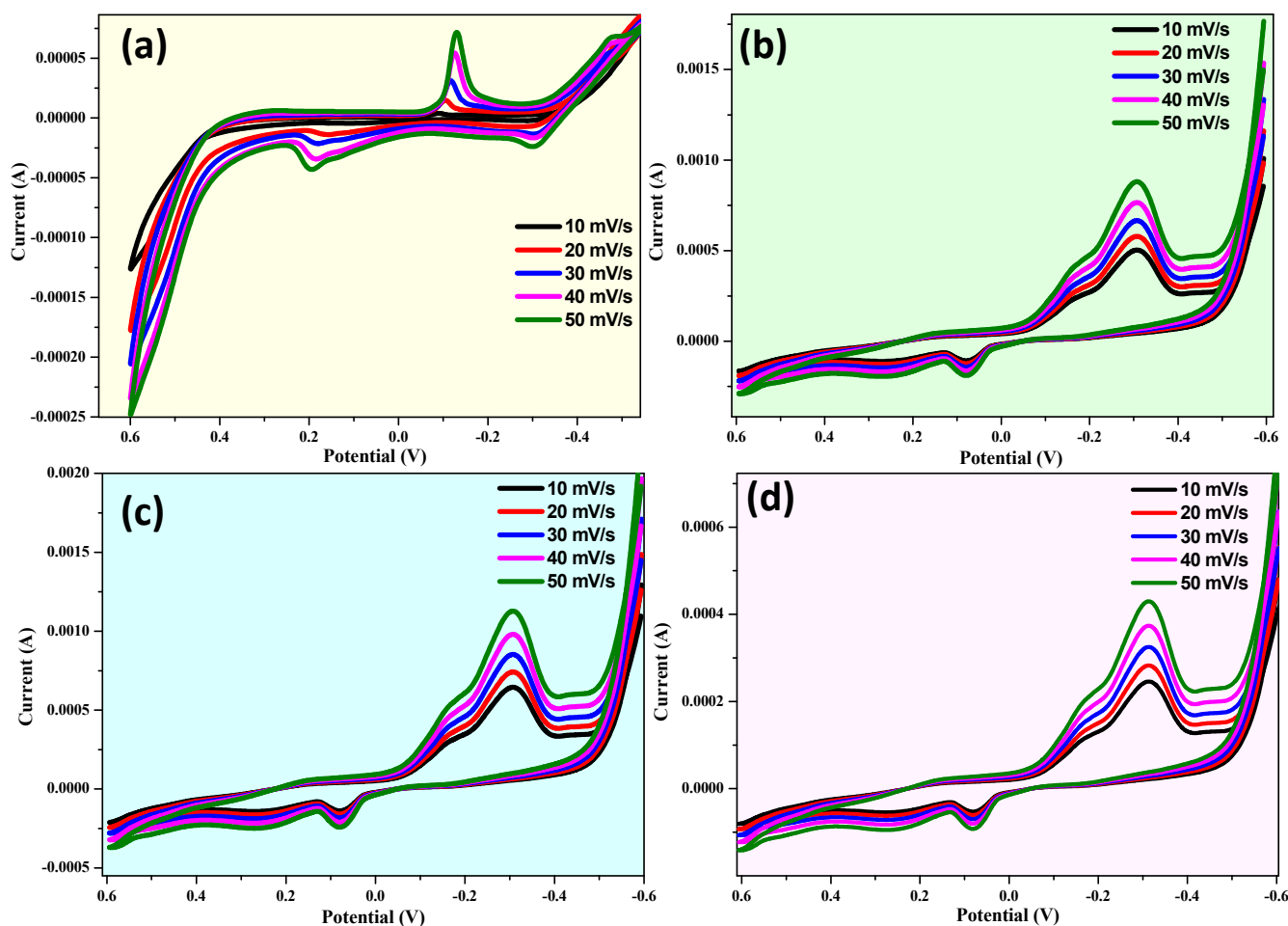


**Figure 11.** Cyclic voltammogram of (a) CuO, (b) CuO + 5% ZnO, (c) CuO + 10% ZnO, and (d) CuO + 15% ZnO samples at various scan rates vs. the Ag/AgCl electrode.

According to the Randles–Sevcik equation for a reversible process, Ref. [90] the height current is symbolized by Equations (23) and (24):

$$i_p = 2.69 \times 10^5 \times n^{3/2} \times A \times D^{1/2} \times C_0 \times v^{1/2} \quad (23)$$

where  $n$ —number of electrons,  $A$ —extent of the electrode,  $D$ —diffusion co-efficient,  $v$ —scanning rate, and  $C_0$ —initial concentration;

$$C_0 = \frac{\rho}{M} \quad (24)$$

where  $\rho$ —is the theoretical density and  $M$ —is the molar mass of samples.

The relation between the cathodic peak current ( $i_p$ ) and the square root of the electrode sample scan rate ( $v^{1/2}$ ) is depicted in Figure 13a–d. The CuO and CuO–ZnO electrode reactions are constrained by hydrogen diffusion, as shown by the strong linear relationship between  $i_p$  and  $\frac{1}{2}$ . Using Equation (1) and the slope of the fitted line in Figure 13, the proton diffusion coefficient ( $D$ ) for CuO, CuO + 5% ZnO, CuO + 10% ZnO, and CuO + 15% ZnO electrode materials calculated to be  $1.470 \times 10^{-5} \text{ cm}^2\text{s}^{-1}$ ,  $1.344 \times 10^{-4} \text{ cm}^2\text{s}^{-1}$ ,  $1.739 \times 10^{-4} \text{ cm}^2\text{s}^{-1}$ , and  $6.525 \times 10^{-5} \text{ cm}^2\text{s}^{-1}$ . Out of which, electrode CuO + 10% ZnO is comparatively greater than the other electrode materials [91–93].

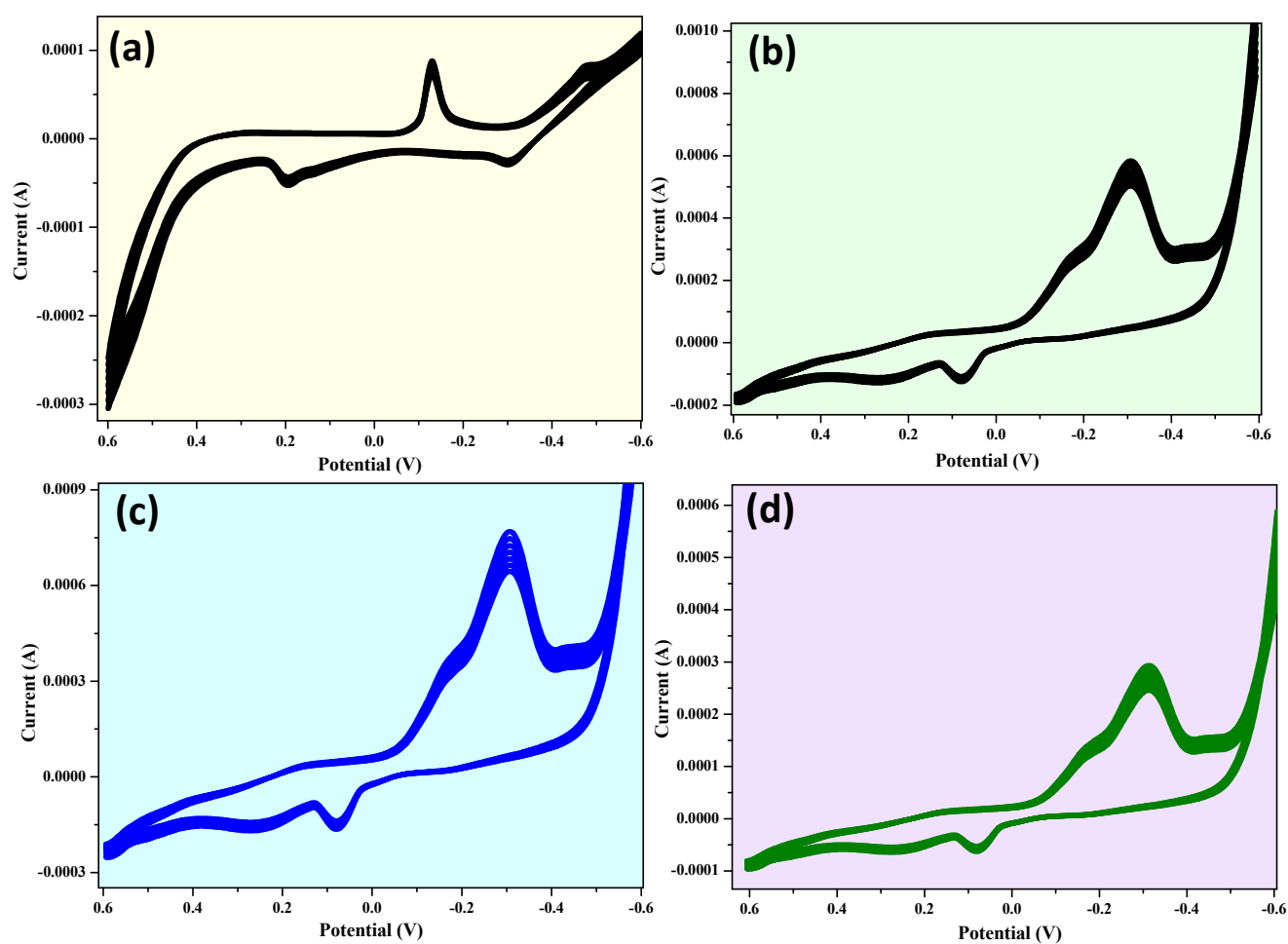


**Figure 12.** Cyclic voltammogram of (a) CuO, (b) CuO + 5% ZnO, (c) CuO + 10% ZnO, and (d) CuO + 15% ZnO electrodes for 25 cycles at 10 mV/s.

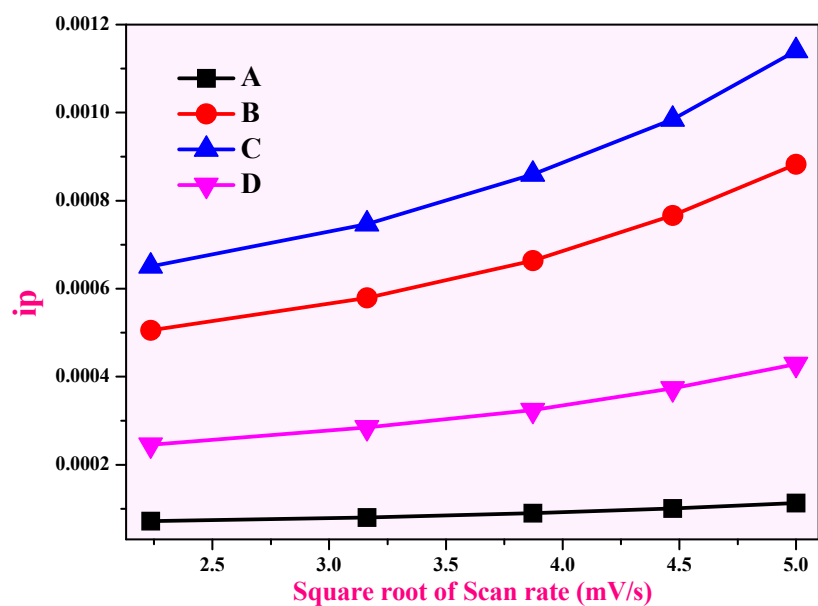


**Figure 13.** Relationship between the anodic peak current ( $i_p$ ) and the square root of the scan rate ( $v^{1/2}$ ) for (A) CuO, (B) CuO + 5% ZnO, (C) CuO + 10% ZnO, and (D) CuO + 15% ZnO.

### 3.2.3. Impedance Spectroscopy Analysis

In Figure 14a–d, the impedance spectra of charge transfer and bulk resistance demonstrated the properties of the prepared electrodes. The creation of a double layer at the electrode–electrolyte interface was confirmed by a nearly vertical line followed by a line with an approximate unity slope in the lower frequency range [94]. We exposed the different parameters, such as charge-transfer resistance ( $R_{ct}$ ) and electrode capacitance ( $C_{dl}$ ), which are tabulated (Table 4) alongside the total capacitance values using an equivalent circuit fitted to a Nyquist plot (Figure 15). The high capacitance and low resistance of an electrode made of CuO and 10% ZnO may result from the electrode's nanocomposite pores being well-matched to the ions in the electrolyte. Table 4 shows the EIS data's for the CuO, CuO + 5% ZnO, CuO + 10% ZnO, and CuO + 15% ZnO electrodes.

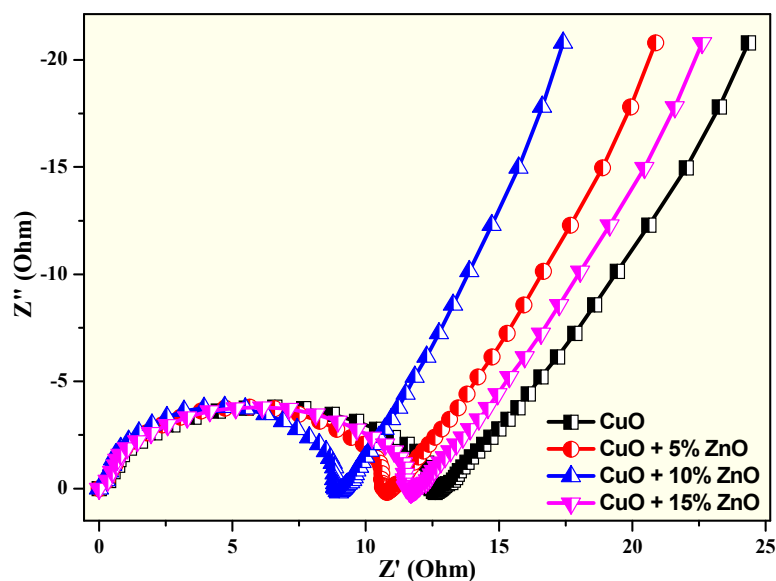


Figure 14. Nyquist plot of CuO, CuO + 5% ZnO, CuO + 10% ZnO, and CuO + 15% ZnO electrodes.

Table 4. EIS data's for CuO, CuO + 5% ZnO, CuO + 10% ZnO, and CuO + 15% ZnO electrodes.

Name of the Electrode	Charge-Transfer Resistance ( $R_{ct}$ ) ( $\Omega$ )	The Capacitance of Double Layer ( $C_{dl}$ ) (F)
CuO	12.52	0.00156
CuO + 5% ZnO	10.61	0.00325
CuO + 10% ZnO	8.34	0.00786
CuO + 15% ZnO	11.96	0.000947

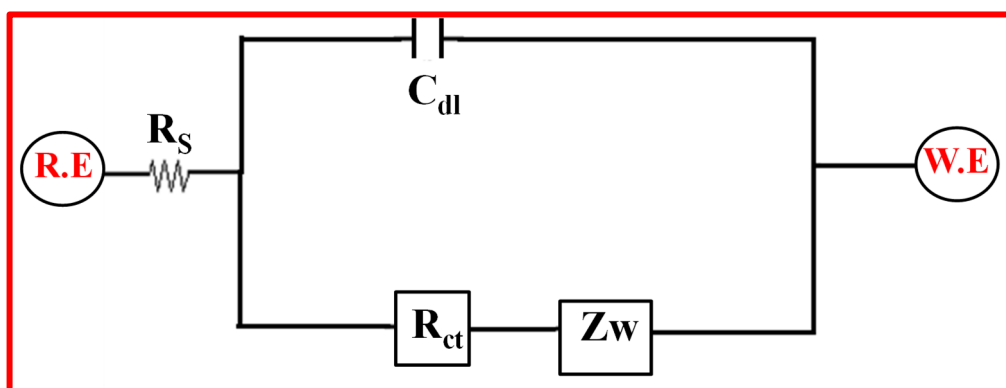


Figure 15. Equivalent circuit of fitted Nyquist plot.

The impedance spectra in Figure 14 were additionally analyzed using a fitting technique with the help of the modified Randal's equivalent circuit that includes  $R_s$  (solution resistance),  $C_{dl}$  (double-layer capacitance),  $R_{ct}$  (charge-transfer resistance), and  $W$  is Warburg component, as shown in Figure 15 [94–96]. The  $R_s$  indicates the resistance of the electrode and current collector.

As observed in the resistance plot, the charge-transfer resistance ( $R_{ct}$ ) and double-layer capacitance ( $C_{dl}$ ) values measure the two-dimensional figure at high frequencies. These plots show that the charge-transfer resistance is low in electrode C, followed by a rise in the electrode's capacitance. From this knowledge, we clarify that electrode C's electrochemical behavior is superior to other electrodes [97–99].

### 3.3. Charge–Discharge Studies

Galvanostatic charge–discharge has been utilized to evaluate the electrochemical behavior of the prepared electrodes (Figure 16). By using Equation (6) [95], the obtained specific capacitance of electrodes A, B, C, and D at 1 A/g current density are 258  $\text{Fg}^{-1}$ , 282  $\text{Fg}^{-1}$ , 368  $\text{Fg}^{-1}$ , and 318  $\text{Fg}^{-1}$ , respectively.

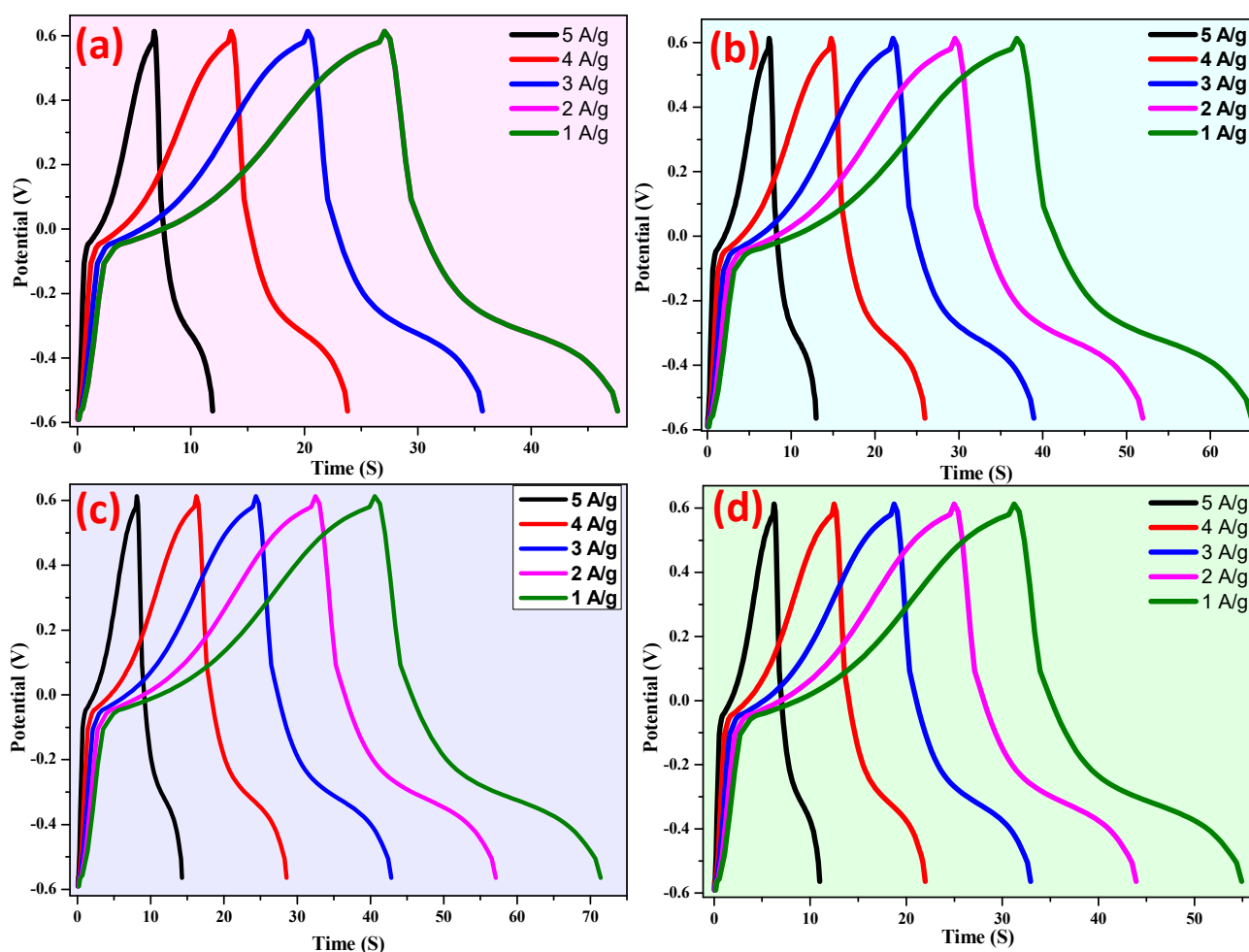
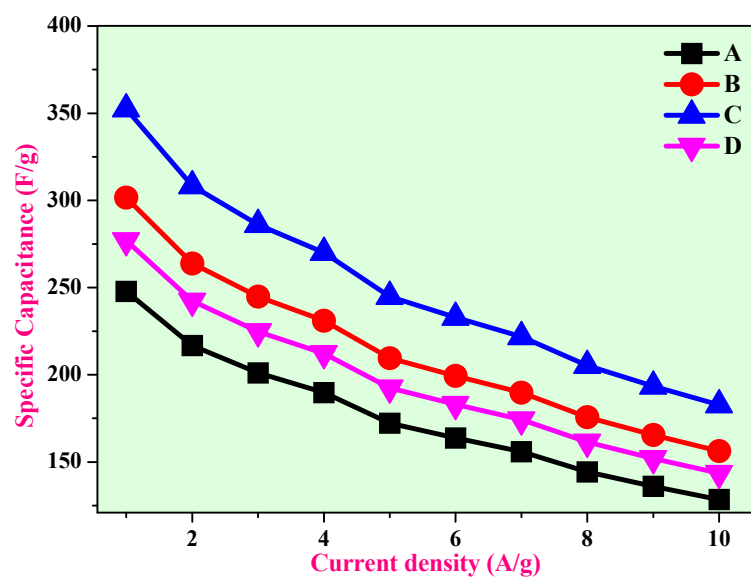


Figure 16. Galvanostatic charge–discharge of (a–d) electrodes at different current densities.

Figure 17 shows the corresponding specific capacitance as a function of current density, which reveals that the specific capacitance decreases for the electrodes with increased current densities. Table 5 illustrates the comparison of capacitance performance of the CuO–ZnO nanocomposite with recent reports. The results clearly show that the CuO–ZnO nanocomposite in the current study has good performance.





**Figure 17.** Variation of the specific capacitance of the electrodes A, B, C, and D as a function of current density.

**Table 5.** Comparison of capacitance performance of CuO-ZnO nanocomposites with recent reports.

S. No	Material	Capacitance (F/g)	References
1	ZnO-CuO	260.7	[99]
2	Carbon-TiO <sub>2</sub>	277	[100]
4	Graphene-ZnO	156	[101]
5	CuO-ZnO	368	Present work

### 3.4. Cyclic Stability

The cycling efficiency of a supercapacitor cell is the most important parameter for the application. The electrochemical cycling stability of the prepared electrodes was carried out. The charge–discharge measurement was repeated 2000 times at a constant 5 A/g current density (Figure 18).

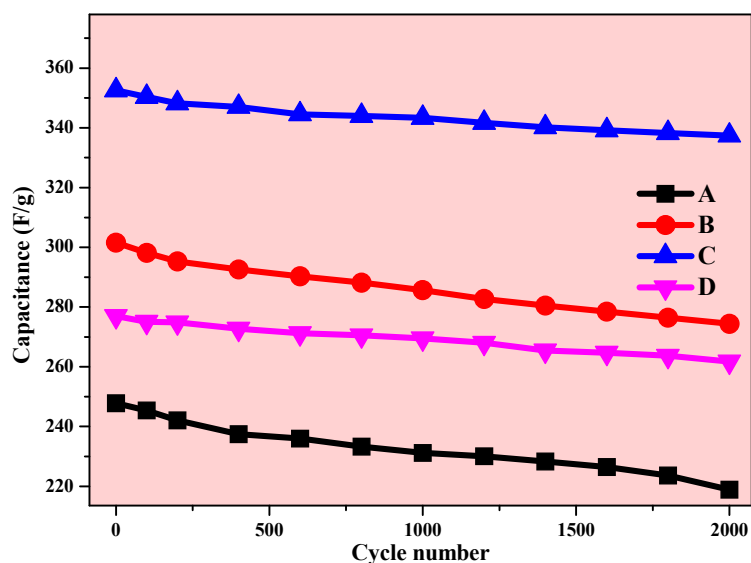


**Figure 18.** Variation of the specific capacitance of electrodes A, B, C, and D as a function of voltametric cycles at 5 A/g current density.

#### 4. Conclusions

For different ratios of CuO and ZnO, two-dimensional CuO-ZnO nanocomposites (NCs) and pure CuO were successfully prepared using the ultrasound-assisted probe sonication method. The structural, photocatalytic, and electrochemical properties were then examined using experimental and theoretical methods. For pure CuO and CuO-ZnO NCs, the XRD (X-ray diffraction) patterns showed a crystallite size ( $D$ ) range of 25 to 31 nm. The sample's optical energy bandgap value ( $E_g$ ) for the NCs was estimated to be between 1.72 and 2.15 eV. The photocatalytic discoloration of pure CuO and CuO-ZnO NCs on fast blue (FB) dye was evaluated under UV light irradiation. The CuO with 10% ZnO composite degraded 83.4% of the dye when exposed to UV radiation, which was more than pure CuO and other composites. Cyclic voltammetry and electrochemical impedance spectroscopy examined the electrochemical characteristics of the synthesized NCs materials (EIS). At 1 A/g current density, the specific capacitance values for CuO, CuO + 5% ZnO, CuO + 10% ZnO, and CuO + 15% ZnO were determined to be  $248 \text{ Fg}^{-1}$ ,  $301 \text{ Fg}^{-1}$ ,  $352 \text{ Fg}^{-1}$ , and  $277 \text{ Fg}^{-1}$ , respectively. During galvanostatic charge–discharge tests, these developed NCs exhibited good capacitance performance in supercapacitor applications. These ground-breaking findings might be considered for scaling up unique resources for dual applications in photocatalysis and supercapacitors.

**Author Contributions:** Conceptualization, M.W.A. and S.M.; data curation, M.W.A.; formal analysis, A.B. and M.F.; funding acquisition, M.W.A.; investigation, A.B.; methodology, A.B., M.F. and N.A.; project administration, M.W.A. and S.M.; resources, M.W.A.; software, M.F., G.M. and S.M.; validation, M.F., G.M. and S.M.; visualization, N.A.; writing—original draft, M.W.A.; writing—review and editing, G.M. and N.A. All authors have read and agreed to the published version of the manuscript.

**Funding:** This work was supported by the Deanship of Scientific Research, Vice Presidency for Graduate Studies and Scientific Research, King Faisal University, Saudi Arabia [Project No: GRANT4222]. The authors would like to acknowledge Princess Nourah bint Abdulrahman University Researchers Supporting Project number (PNURSP2023R230), Princess Nourah bint Abdulrahman University, Riyadh, Saudi Arabia.

**Institutional Review Board Statement:** Not applicable.

**Informed Consent Statement:** Not applicable.

**Data Availability Statement:** Not applicable.

**Conflicts of Interest:** The authors declare no conflict of interest.

#### References

1. Conway, B.E. *Electrochemical Supercapacitors: Scientific Fundamentals and Technological Applications*; Springer: Berlin/Heidelberg, Germany, 1999.
2. Burke, A. Ultracapacitors: Why, how, and where is the technology. *J. Power Sources* **2000**, *91*, 37–50. [[CrossRef](#)]
3. Zhang, L.L.; Zhao, X.S. Carbon-based materials as supercapacitor electrodes. *Chem. Soc. Rev.* **2009**, *38*, 2520–2531. [[CrossRef](#)] [[PubMed](#)]
4. Winter, M.; Brodd, R.J. What are batteries, fuel cells, and supercapacitors. *Chem. Rev.* **2004**, *104*, 4245–4269. [[CrossRef](#)] [[PubMed](#)]
5. Miller, J.R.; Simon, P. Electrochemical capacitors for energy management. *Science* **2008**, *321*, 651–652. [[CrossRef](#)]
6. Alam, M.W.; Al Qahtani, H.S.; Souayah, B.; Ahmed, W.; Albalawi, H.; Farhan, M.; Abuzir, A.; Naeem, S. Novel copper-zinc-manganese ternary metal oxide nanocomposite as heterogeneous catalyst for glucose sensor and antibacterial activity. *Antioxidants* **2022**, *11*, 1064. [[CrossRef](#)]
7. Cai, J.; Niu, H.; Li, Z.; Du, Y.; Cizek, P.; Xie, Z.; Xiong, H.; Lin, T. High-performance supercapacitor electrode materials from cellulose-derived carbon nanofibers. *ACS Appl. Mater. Interfaces* **2015**, *7*, 14946–14953. [[CrossRef](#)]
8. Nie, Y.F.; Wang, Q.; Chen, X.Y.; Zhang, Z.J. Synergistic effect of novel redox additives of p-nitroaniline and dimethylglyoxime for highly improving the supercapacitor performances. *Phys. Chem. Chem. Phys.* **2016**, *18*, 2718–2729. [[CrossRef](#)]
9. Lam, L.T.; Louey, R. Development of ultra-battery for hybrid-electric vehicle applications. *J. Power Sources* **2006**, *158*, 1140–1148. [[CrossRef](#)]
10. Stoller, M.D.; Park, S.; Zhu, Y.; An, J.; Ruoff, R.S. Graphene-based ultracapacitors. *Nano Lett.* **2008**, *8*, 3498–3502. [[CrossRef](#)]
11. Xu, G.; Zheng, C.; Zhang, Q.; Huang, J.; Zhao, M.; Nie, J.; Wang, X.; Wei, F. Binder-free activated carbon/carbon nanotube paper electrodes for use in supercapacitors. *Nano Res.* **2011**, *4*, 870–881. [[CrossRef](#)]

12. Zheng, C.; Zhou, X.; Cao, H.; Wang, G.; Liu, Z. Synthesis of porous graphene/activated carbon composite with high packing density and large specific surface area for supercapacitor electrode material. *J. Power Sources* **2014**, *258*, 290–296. [\[CrossRef\]](#)
13. JSieben, J.; Morallón, E.; Cazorla-Amorós, D. Flexible ruthenium oxide-activated carbon cloth composites prepared by simple Electrodeposition methods. *Energy* **2013**, *58*, 519–526. [\[CrossRef\]](#)
14. Alam, M.W.; Azam, H.; Khalid, N.R.; Naeem, S.; Hussain, M.K.; BaQais, A.; Farhan, M.; Souayah, B.; Zaidi, N.; Khan, K. Enhanced photocatalytic performance of Ag<sub>3</sub>PO<sub>4</sub>/Mn-ZnO nanocomposite for the degradation of Tetracycline Hydrochloride. *Crystals* **2022**, *12*, 1156. [\[CrossRef\]](#)
15. Lota, K.; Sierczynska, A.; Lota, G. Supercapacitors based on nickel oxide/carbon materials composites. *Int. J. Electrochem.* **2011**, *2011*, 321473. [\[CrossRef\]](#)
16. Hu, C.; He, S.; Jiang, S.; Chen, S.; Hou, H. Natural source derived carbon paper supported conducting polymer nanowire arrays for high performance supercapacitors. *RSC Adv.* **2015**, *5*, 14441–14447. [\[CrossRef\]](#)
17. Shi, Y.; Pan, L.; Liu, B.; Wang, Y.; Cui, Y.; Bao, Z.; Yu, G. Nanostructured conductive polypyrrole hydrogels as high-performance flexible supercapacitor electrodes. *J. Mater. Chem. A* **2014**, *2*, 6086–6091. [\[CrossRef\]](#)
18. Cozzoli, P.D.; Kornowski, A.; Weller, H. Low-temperature synthesis of soluble and processable organic-capped anatase TiO<sub>2</sub> nanorods. *J. Am. Chem. Soc.* **2003**, *125*, 14539–14548. [\[CrossRef\]](#) [\[PubMed\]](#)
19. Hu, C.C.; Chang, K.H.; Lin, M.C.; Wu, Y.T. Design and tailoring of the nanotubular arrayed architecture of hydrous RuO<sub>2</sub> for next generation supercapacitors. *Nano Lett.* **2006**, *6*, 2690–2695. [\[CrossRef\]](#)
20. Sahay, R.; Kumar, P.S.; Aravindan, V.; Sundaramurthy, J.; Ling, W.C.; Mhaisalkar, S.G.; Ramakrishna, S.; Madhavi, S. High aspect ratio electro spun CuO nano fibers as anode material for lithium-ion batteries with superior cycle ability. *J. Phys. Chem. C* **2012**, *116*, 18087–18092. [\[CrossRef\]](#)
21. Waqas Alam, M.; Khatoon, U.; Qurashi, A. Synthesis and characterization of Cu-SnO<sub>2</sub> nanoparticles deposited on glass using ultrasonic spray pyrolysis and their H<sub>2</sub>S sensing properties. *Curr. Nanosci.* **2012**, *8*, 919–924. [\[CrossRef\]](#)
22. Liang, C.; Gao, M.; Pan, H.; Liu, Y.; Yan, M. Lithium alloys and metal oxides as high-capacity anode materials for lithium-ion batteries. *J. Alloys Compd.* **2013**, *575*, 246–256. [\[CrossRef\]](#)
23. Shaikh, J.S.; Pawar, R.C.; Moholkar, A.V.; Kim, J.H.; Patil, P.S. CuO-PAA hybrid films: Chemical synthesis and supercapacitor behaviour. *Appl. Surf. Sci.* **2011**, *257*, 4389–4397. [\[CrossRef\]](#)
24. Chandekar, K.V.; Shkir, M.; Al-Shehri, B.M.; Al Faifyb, S.; Halor, R.G.; Khane, A.; Al-Namshah, K.S.; Hamdy, M.S. Visible light sensitive Cu doped ZnO: Facile synthesis, characterization and high photocatalytic response. *Mater. Charact.* **2020**, *165*, 110387. [\[CrossRef\]](#)
25. Zhang, T.; Tang, X.; Zhang, J.; Zhou, T.; Wang, H.; Wu, C.; Xia, X.; Xie, C.; Zeng, D. Preparation, characterization and photocatalytic performance of heterostructured CuO–ZnO-loaded composite nanofiber membranes. *Langmuir* **2018**, *34*, 14577–14585. [\[CrossRef\]](#) [\[PubMed\]](#)
26. Sivasankar, K.; Rani, K.K.; Wang, S.-F.; Devasenathipathy, R.; Lin, C.-H. Copper Nanoparticle and Nitrogen Doped Graphite Oxide Based Biosensor for the Sensitive Determination of Glucose. *Nanomaterials* **2018**, *8*, 429. [\[CrossRef\]](#) [\[PubMed\]](#)
27. Chen, J.T.; Zhang, F.; Wang, J.; Zhang, G.A.; Miao, B.B.; Fan, X.Y.; Yan, D.; Yan, P.X. CuO nanowires synthesized by thermal oxidation route. *J. Alloys Compd.* **2008**, *454*, 268. [\[CrossRef\]](#)
28. Dierstein, A.; Natter, H.; Meyer, F.; Stephan, H.O.; Kropf, C.; Hempelmann, R. Electrochemical deposition under oxidizing conditions (EDOC): A new synthesis for nanocrystalline metal oxides. *Scr. Mater.* **2001**, *44*, 2209. [\[CrossRef\]](#)
29. Yu, L.; Zhang, G.; Wu, Y.; Bai, X.; Guo, D. Cupric oxide nanoflowers synthesized with a simple solution route and their field emission. *J. Cryst. Growth* **2008**, *310*, 3125. [\[CrossRef\]](#)
30. Zhu, J.; Bi, H.; Wang, Y.; Wang, X.; Yang, X.; Lu, L. Synthesis of flower-like CuO nanostructures via a simple hydrolysis route. *Mater. Lett.* **2007**, *61*, 5236. [\[CrossRef\]](#)
31. Su, Y.K.; Shen, C.M.; Yang, H.T.; Li, H.L.; Gao, H.J. Controlled synthesis of highly ordered CuO nanowire arrays by template-based sol-gel route. *Trans. Nonferrous Met. Soc. China* **2007**, *17*, 783. [\[CrossRef\]](#)
32. Han, D.; Yang, H.; Zhu, C.; Wang, F. Controlled synthesis of CuO nanoparticles using TritonX-100-based water-in-oil reverse micel. *Powder Technol.* **2008**, *185*, 286. [\[CrossRef\]](#)
33. Tang, X.L.; Ren, L.; Sun, L.N.; Tian, W.G.; Cao, M.H.; Hu, C.W. A solvothermal route to Cu<sub>2</sub>O nanocubes and Cu nanoparticles. *Chem. Res. Chin. Univ.* **2006**, *22*, 551. [\[CrossRef\]](#)
34. Song, X.; Yu, H.; Sun, S.L. Single-crystalline CuO nanobelts fabricated by a convenient route. *J. Colloid Interface Sci.* **2005**, *289*, 591. [\[CrossRef\]](#) [\[PubMed\]](#)
35. Keyson, D.; Volanti, D.P.; Cavalcante, L.S.; Simes, A.Z.; Varela, J.A.; Longo, E. CuO urchin-nanostructures synthesized from a domestic hydrothermal microwave method. *Mater. Res. Bull.* **2008**, *43*, 775. [\[CrossRef\]](#)
36. Xu, X.; Zhang, M.; Feng, J.; Zhang, M. Shape-controlled synthesis of single-crystalline cupric oxide by microwave heating using an ionic liquid. *Mater. Lett.* **2008**, *62*, 2790. [\[CrossRef\]](#)
37. Melghit, K.; Wen, L.S. The effect of starting materials on the morphology and particle size of copper pyrovanadate Cu<sub>3</sub>V<sub>2</sub>O<sub>7</sub>(OH)<sub>2</sub>·2H<sub>2</sub>O. *Ceram. Int.* **2005**, *31*, 223. [\[CrossRef\]](#)
38. Almasian, A.; Mahmoodi, N.M.; Olya, M.E. Tectomer grafted nanofiber: Synthesis, characterization and dye removal ability from multicomponent system. *J. Ind. Eng. Chem.* **2015**, *32*, 85–98. [\[CrossRef\]](#)

39. Mahmoodi, N.M.; Ghezelbash, M.; Shabanian, M.; Aryanasab, F.; Saeb, M.R. Efficient removal of cationic dyes from colored wastewaters by dithiocarbamate-functionalized graphene oxide nanosheets: From synthesis to detailed kinetics studies. *J. Taiwan Inst. Chem. Eng.* **2017**, *81*, 239–246. [\[CrossRef\]](#)
40. Hosseini, F.; Sadighian, S.; Hosseini-Monfared, H.; Mahmoodi, N.M. Dye removal and kinetics of adsorption by magnetic chitosan nanoparticles. *Desalination Water Treat.* **2016**, *57*, 24378–24386. [\[CrossRef\]](#)
41. Shilpa Amulya, M.A.; Nagaswarupa, H.P.; Anil Kumar, M.R.; Ravikumar, C.R.; Kusuma, K.B. Sonochemical synthesis of  $\text{MnFe}_2\text{O}_4$  nanoparticles and their electrochemical and photocatalytic properties. *J. Phys. Chem. Solids* **2021**, *148*, 109661. [\[CrossRef\]](#)
42. Siddiqui, V.U.; Ansari, A.; Taazeem Ansari, M.; Akram, M.K.; Siddiqi, W.A.; Alosaimi, A.M.; Hussein, M.A.; Rafatullah, M. Optimization of Facile Synthesized ZnO/CuO Nanophotocatalyst for Organic Dye Degradation by Visible Light Irradiation Using Response Surface Methodology. *Catalysts* **2021**, *11*, 1509. [\[CrossRef\]](#)
43. Abebe, B.; Tsegaye, D.; Sori, C.; Prasad, R.C.K.R.; Murthy, H.C.A. Cu/CuO-Doped ZnO Nanocomposites via Solution Combustion Synthesis for Catalytic 4-Nitrophenol Reduction. *ACS Omega* **2023**, *8*, 9597–9606. [\[CrossRef\]](#) [\[PubMed\]](#)
44. Wu, F.; Wang, X.; Hu, S.; Hao, C.; Gao, H.; Zhou, S. Solid-state preparation of CuO/ZnO nanocomposites for functional supercapacitor electrodes and photocatalysts with enhanced photocatalytic properties. *Int. J. Hydrog. Energy* **2017**, *42*, 30098–30108. [\[CrossRef\]](#)
45. Sivakumar, S.; Robinson, Y.; Mala, N.A. Studies on Photocatalytic Performance and Supercapacitor Applications of Undoped and Cu-Doped ZnO Nanoparticles. *Appl. Surf. Sci. Adv.* **2022**, *12*, 100344. [\[CrossRef\]](#)
46. Brahma, S.; Yeh, Y.-W.; Huang, J.-L.; Liu, C.-P. Cu-Doped p-Type ZnO Nanostructures as Unique Acetone Sensor at Room Temperature ( $\sim 25^\circ\text{C}$ ). *Appl. Surf. Sci.* **2021**, *564*, 150351. [\[CrossRef\]](#)
47. Nadargi, D.Y.; Tamboli, M.S.; Patil, S.S.; Dateer, R.B.; Mulla, I.S.; Choi, H.; Suryavanshi, S.S. Microwave-Epoxy-Assisted Hydrothermal Synthesis of the CuO/ZnO Heterojunction: A Highly Versatile Route to Develop  $\text{H}_2\text{S}$  Gas Sensors. *ACS Omega* **2020**, *5*, 8587–8595. [\[CrossRef\]](#)
48. Alam, M.W.; Aamir, M.; Farhan, M.; Albuhulayqah, M.; Ahmad, M.M.; Ravikumar, C.R.; Dileep Kumar, V.G.; Ananda Murthy, H.C. Green Synthesis of Ni-Cu-Zn Based Nanosized Metal Oxides for Photocatalytic and Sensor Applications. *Crystals* **2021**, *11*, 1467. [\[CrossRef\]](#)
49. Paraguay-Delgado, F.; Hermida-Montero, L.A.; Morales-Mendoza, J.E.; Durán-Barradas, Z.; Mtz-Enriquez, A.I.; Pariona, N. Photocatalytic Properties of Cu-Containing ZnO Nanoparticles and Their Antifungal Activity against Agriculture-Pathogenic Fungus. *RSC Adv.* **2022**, *12*, 9898–9908. [\[CrossRef\]](#)
50. Mahmoud, A.; Echabaane, M.; Omri, K.; Boudon, J.; Saviot, L.; Millot, N.; Chaabane, R.B. Cu-Doped ZnO Nanoparticles for Non-Enzymatic Glucose Sensing. *Molecules* **2021**, *26*, 929. [\[CrossRef\]](#)
51. Mohan, R.; Krishnamoorthy, K.; Kim, S.J. Enhanced photocatalytic activity of Cu-doped ZnO nanorods. *Solid State Commun.* **2012**, *152*, 375–380. [\[CrossRef\]](#)
52. Fu, M.; Li, Y.; Lu, P.; Liu, J.; Dong, F. Sol-gel preparation and enhanced photocatalytic performance of Cu-doped ZnO nanoparticles. *Appl. Surf. Sci.* **2011**, *258*, 1587–1591. [\[CrossRef\]](#)
53. Panahi-Kalamuei, M.; Mousavi-Kamazani, M.; Salavati-Niasari, M.; Hosseinpour-Mashkani, S.M. A simple sonochemical approach for synthesis of selenium nanostructures and investigation of its light harvesting application. *Ultrason. Sonochem.* **2015**, *23*, 246. [\[CrossRef\]](#) [\[PubMed\]](#)
54. Mamatha, K.M.; Ravikumar, C.R.; Murthy, H.A.; Kumar, V.D.; Kumar, A.N.; Jahagirdar, A.A. Facile green synthesis of Molybdenum oxide nanoparticles using Centella Asiatica plant: Its photocatalytic and electrochemical lead sensor applications. *Sens. Int.* **2022**, *3*, 100153. [\[CrossRef\]](#)
55. Mousavi-Kamazani, M.; Rahmatolahzadeh, R.; Shobeiri, S.A.; Beshkar, F. Sonochemical synthesis, formation mechanism, and solar cell application of tellurium nanoparticles. *Ultrason. Sonochem.* **2017**, *39*, 233. [\[CrossRef\]](#)
56. Saravanakkumar, D.; Oualid, H.A.; Brahmi, Y.; Ayeshamariam, A.; Karunanaithy, M.; Saleem, A.M.; Kaviyarasu, K.; Sivaranjani, S.; Jayachandran, M. Synthesis and characterization of CuO/ZnO/CNTs thin films on copper substrate and its photocatalytic applications. *Open Nano* **2019**, *4*, 100025. [\[CrossRef\]](#)
57. Yadav, M.S.; Tripathi, S.K. Synthesis and characterization of nanocomposite NiO/activated charcoal electrodes for supercapacitor application. *Ionics* **2017**, *23*, 2919–2930. [\[CrossRef\]](#)
58. Yesuraj, J.; Elumalai, V.; Bhagavathiachari, M.; Samuel, A.S.; Elaiyappillai, E.; Johnson, P.M. A facile sonochemical assisted synthesis of  $\alpha\text{-MnMoO}_4$ /PANI nanocomposite electrode for supercapacitor applications. *J. Electroanal. Chem.* **2017**, *797*, 78–88. [\[CrossRef\]](#)
59. Fanga, J.; Xuan, Y. Investigation of optical absorption and photothermal conversion characteristics of binary CuO/ZnO nanofluids. *RSC Adv.* **2017**, *7*, 56023. [\[CrossRef\]](#)
60. Sahu, S.; Samanta, P.K. Peak Profile Analysis of X-ray Diffraction Pattern of Zinc Oxide Nanostructure. *J. Nano Electron. Phys.* **2021**, *13*, 05001. [\[CrossRef\]](#)
61. Inamdar, A.I.; Kim, Y.S.; Sohn, J.S.; Im, H.; Kim, H.; Kim, D.-Y.; Kalubarme, R.S.; Park, C. Supercapacitive Characteristics of Electrodeposited Polyaniline Thin Films Grown on Indium-doped Tin-oxide Substrates. *J. Korean Phys. Soc.* **2011**, *59*, 145–149. [\[CrossRef\]](#)
62. Cullity, B.D. *Elements of X-ray Diffraction*; Addison-Wesley: Boston, MA, USA, 1956.



63. Lee, J.B.; Lee, H.J.; Seo, S.H.; Park, J.S. Characterization of undoped and Cu doped ZnO film for surface acoustic wave applications. *Thin Solid Film.* **2001**, *398*, 641–646. [\[CrossRef\]](#)
64. Sharma, P.K.; Kumar, M.; Pandey, A.C. Green luminescent ZnO: Cu<sup>2+</sup> nanoparticles and their applications in white light generation from UV LEDs. *J. Nanopart. Res.* **2011**, *13*, 1629–1637. [\[CrossRef\]](#)
65. Che, C.; Liu, X.; Fang, Q.; Chen, X.; Liu, T.; Zhang, M. Self-assembly synthesis of CuO/ZnO hollow microspheres and their photocatalytic performance under natural sunlight. *Vacuum* **2020**, *174*, 109198.
66. Shilpa Amulya, M.A.; Nagaswarupa, H.P.; Anil Kumar, M.R.; Ravikumar, C.R.; Kusuma, K.B. Enhanced photocatalytic and electrochemical properties of Cu doped NiMnFe<sub>2</sub>O<sub>4</sub> nanoparticles synthesized via probe sonication method. *Appl. Surf. Sci. Adv.* **2020**, *2*, 100038. [\[CrossRef\]](#)
67. Devi, A.B.; Moirangthem, D.S.; Talukdar, N.C.; Devi, M.D.; Singh, N.R.; Luwang, M.N. Novel synthesis and characterization of CuO nanomaterials: Biological applications. *Chin. Chem. Lett.* **2014**, *25*, 1615–1619. [\[CrossRef\]](#)
68. Rudresha, K.; Zahir Hussain, A.; Ravikumar, C.R.; Anil Kumar, M.R.; Nagaswarupa, H.P.; Santosh, M.S.; Ananda Murthy, H.C. Synthesis and Characterization of green CuO using Centella Asiatica plant leaf extract: Electrochemical and Photocatalytic activities. *Adv. Mater. Lett.* **2020**, *11*, 121586. [\[CrossRef\]](#)
69. Kumar, A.N.; Jnaneshwara, D.; Ravikumar, C.; Kumar, M.A.; Murthy, H.A.; Shekhar, T.S.; Jahagirdar, A. La<sub>10</sub>Si<sub>6</sub>O<sub>27</sub>: Tb<sup>3+</sup> nanomaterial; Its Photocatalytic and Electrochemical Sensor Activities on Disperse Orange and Fast Blue dyes. *Sens. Int.* **2020**, *2*, 100076. [\[CrossRef\]](#)
70. Abebe, B.; Ravikumar, C.R.; Zereffa, E.A.; Kumar, A.N.; Murthy, H.C.A. Photocatalytic and superior ascorbic acid sensor activities of PVA/Zn-Fe-Mn ternary oxide nanocomposite. *Inorg. Chem. Commun.* **2021**, *123*, 108343. [\[CrossRef\]](#)
71. Avinash, B.; Ravikumar, C.R.; Kumar, M.A.; Santosh, M.S.; Pratapkumar, C.; Nagaswarupa, H.P.; Murthy, H.A.; Deshmukh, V.V.; Bhatt, A.S.; Jahagirdar, A.A.; et al. NiO bio-composite materials: Photocatalytic, electrochemical and supercapacitor applications. *Appl. Surf. Sci. Adv.* **2021**, *3*, 100049. [\[CrossRef\]](#)
72. Basavaraju, N.; Prashantha, S.C.; Nagabhushana, H.; Naveen Kumar, A.; Chandrasekhar, M.; Shashi Shekhar, T.R.; Ravikumar, C.R.; Anil Kumar, M.R.; Surendra, B.S.; Nagaswarupa, H.P. Luminescent and thermal properties of novel orange–red emitting MgNb<sub>2</sub>O<sub>6</sub>: Sm<sup>3+</sup> phosphors for displays, photo catalytic and sensor applications. *SN Appl. Sci.* **2021**, *3*, 100049. [\[CrossRef\]](#)
73. Ranjitha, R.; Meghana, K.N.; Kumar, V.G.D.; Bhatt, A.S.; Jayanna, B.K.; Ravikumar, C.R.; Santosh, M.S.; Madhyastha, H.; Sakai, K. Rapid photocatalytic degradation of cationic organic dyes using Li-doped Ni/NiO nanocomposites and their electrochemical performance. *New J. Chem.* **2021**, *2*, 796. [\[CrossRef\]](#)
74. Raghavendra, N.; Nagaswarupa, H.P.; Shashi Shekhar, T.R.; Mylarappa, M.; Surendra, B.S.; Prashantha, S.C.; Basavaraju, N.; Ravi Kumar, C.R.; Anil Kumar, M.R. Electrochemical sensor studies and optical analysis of developed clay based CoFe<sub>2</sub>O<sub>4</sub> ferrite NPs. *Sens. Int.* **2021**, *2*, 100083. [\[CrossRef\]](#)
75. Bhuvan Raj, N.; Pavithra Gowda, N.T.; Pooja, O.S.; Purushotham, B.; Anil Kumar, M.R.; Sukrutha, S.K.; Ravikumar, C.R.; Nagaswarupa, H.P.; Ananda Murthy, H.C.; Boppana, S.B. Harnessing ZnO nanoparticles for antimicrobial and photocatalytic activities. *J. Photochem. Photobiol.* **2021**, *6*, 100021.
76. Raghavendra, N.; Nagaswarupa, H.P.; Shashi Shekhar, T.R.; Mylarappa, M.; Surendra, B.S.; Prashantha, S.C.; Ravikumar, C.R.; Anil Kumar, M.R.; Basavaraju, N. Development of clay ferrite nanocomposite: Electrochemical, sensors and photocatalytic studies. *Appl. Surf. Sci. Adv.* **2021**, *5*, 100103. [\[CrossRef\]](#)
77. Kusuma, K.B.; Manju, M.; Ravikumar, C.R.; Dileepkumar, V.G.; Kumar, A.N.; Santosh, M.S.; Murthy, H.A.; Gurushantha, K. Probe Sonicated synthesis of Bismuth oxide (Bi<sub>2</sub>O<sub>3</sub>) nanoparticles: Photocatalytic application and Electrochemical sensing of Ascorbic acid lead. *J. Nanomater.* **2022**, *2022*, 3256611. [\[CrossRef\]](#)
78. Kumar, V.D.; Balaji, K.; Viswanatha, R.; Ambika, G.; Roopa, R.A.; Basavaraja, B.M.; Chennabasappa, M.; Kumar, C.R.; Chen, Z.; Bui, X.; et al. Visible light photodegradation of 2,4-dichlorophenol using nanostructured NaBiS<sub>2</sub>: Kinetics, cytotoxicity, antimicrobial and electrochemical studies of the photocatalyst. *Chemosphere* **2022**, *287*, 132174. [\[CrossRef\]](#)
79. Alam, M.W.; Kumar, V.G.D.; Ravikumar, C.R.; Prashantha, S.C.; Murthy, H.C.A.; Kumar, M.R.A. Chromium (III) doped polycrystalline MgAl<sub>2</sub>O<sub>4</sub> nanoparticles for photocatalytic and supercapacitor applications. *J. Phys. Chem. Solids* **2022**, *161*, 110491. [\[CrossRef\]](#)
80. Shashank, M.; Naik, H.B.; Patil, S.B.; Viswantha, R.; Nagaraju, G. Green synthesis of molybdenum oxide nanoparticles: Advanced electrode material for electrochemical lithium storage. *Microchem. J.* **2021**, *171*, 106818. [\[CrossRef\]](#)
81. Kumar, M.A.; Abebe, B.; Nagaswarupa, H.P.; Murthy, H.A.; Ravikumar, C.R.; Sabir, F.K. Enhanced photocatalytic and electrochemical performance of TiO<sub>2</sub>-Fe<sub>2</sub>O<sub>3</sub> nanocomposite: Its applications in dye decolorization and as supercapacitors. *Sci. Rep. Nat.* **2020**, *10*, 1249. [\[CrossRef\]](#)
82. Masunga, N.; Mmesesi, O.K.; Kefeni, K.K.; Mamba, B.B. Recent advances in copper ferrite nanoparticles and nanocomposites synthesis, magnetic properties and application in water treatment: Review. *J. Environ. Chem. Eng.* **2019**, *7*, 103179. [\[CrossRef\]](#)
83. Bekru, A.G.; Tufa, L.T.; Zelekew, O.A.; Goddati, M.; Lee, J.; Sabir, F.K. Green Synthesis of a CuO-ZnO Nanocomposite for Efficient Photodegradation of Methylene Blue and Reduction of 4-Nitrophenol. *ACS Omega* **2022**, *7*, 30908–30919. [\[CrossRef\]](#) [\[PubMed\]](#)
84. Bhat, A.H.; Chisti, H.T.N. Facile Fabrication of Ternary Metal Oxide ZnO/CuO/SnO<sub>2</sub> Nanocomposite for Excellent Photocatalytic degradation of Fast Green Dye. *Int. J. Environ. Anal. Chem.* **2021**, *1–22*. [\[CrossRef\]](#)
85. Alzahrani, E. Chitosan Membrane Embedded with ZnO/CuO Nanocomposite for the Photodegradation of Fast Green Dye Under Artificial and Solar Irradiation. *Analytical Chem. Insights* **2018**, *13*, 1177390118763361. [\[CrossRef\]](#)



86. Ataabadi, M.R.; Jamshidi, M. Silane modification of TiO<sub>2</sub> nanoparticles and usage in acrylic film for effective photocatalytic degradation of methylene blue under visible light. *Sci. Rep.* **2023**, *13*, 7383. [[CrossRef](#)] [[PubMed](#)]
87. Manjula, S.N.; Chandrasekhar, M.; Naik, R.; Revathi, V.; Nagabhushana, H.; Ravikumar, C.R.; Surendra, B.S.; Kumar, A.N. Low temperature synthesized MgAl<sub>2</sub>O<sub>4</sub>:Eu<sup>3+</sup> nanophosphors and its structural validations using DFT: Photoluminescent, Photocatalytic and Electrochemical properties of multifunctional applications. *Lumin. J. Biol. Chem. Lumin.* **2022**, *38*, 1149–1166.
88. Naik, R.; Kumar, A.N.; Shanbhag, V.; Ravikumar, C.R.; Revathi, V.; Basavaraju, N.; Prashantha, S.C.; Girish, K.M.; Nagabhushana, H. Aloe barbadensis Mill leaf gel assisted combustion synthesized ZnO:Ni<sup>3+</sup> Electrochemical sensor for ascorbic acid detection and photocatalysis. *Inorg. Chem. Commun.* **2022**, *143*, 100153. [[CrossRef](#)]
89. Shruthi, B.; Madhu, B.J.; Bheema Raju, V. Influence of TiO<sub>2</sub> on the electrochemical performance of pasted type β-nickel hydroxide electrode in alkaline electrolyte. *J. Energy Chem.* **2016**, *25*, 41–48. [[CrossRef](#)]
90. Dhananjaya, N.; Ambujakshi, N.P.; Ravikumar, C.R.; Naveen Kumar, A. Comparative study on photocatalytic degradation and sensor properties of Chonemorpha fragrans leaf extract assisted Mg<sub>x</sub>Zn<sub>1-x</sub>O (0 ≤ x ≤ 1) nanoparticles. *Inorg. Chem. Commun.* **2022**, *144*, 109827. [[CrossRef](#)]
91. Rudresha, K.; Zahir Hussain, A.; Ravikumar, C.R.; Anil Kumar, M.R.; Naveen Kumar, A.; Manjunatha, A.S.; Nagaswarupa, H.P.; Shilpa Amulya, M.A.; Ananda Murthy, H.C. UV light Assisted De-colorization of Dyes and electrochemical Sensing of Arsenic by CuO–ZnO Hybrid Nanocomposite synthesized via sonication method. *J. Phys. Chem. Solids* **2022**, *144*, 109827.
92. Kong, L.; Yan, Q.; Wang, Y.; Wang, Q.; Andrews, C.B.; Zheng, C. Self-supported trimetallic NiZnLa nanosheets on hierarchical porous graphene oxide-polymer composite fibers for enhanced phosphate removal from water. *J. Colloid Interface Sci.* **2022**, *628*, 807–818. [[CrossRef](#)]
93. Martin, P. Andersson Entropy reduction from strong localization an explanation for enhanced reaction rates of organic synthesis in aqueous micelles. *J. Colloid Interface Sci.* **2022**, *628*, 819–828.
94. Tayyab, M.; Liu, Y.; Liu, Z.; Xu, Z.; Yue, W.; Zhou, L.; Lei, J.; Zhang, J. A new breakthrough in photocatalytic hydrogen evolution by amorphous and chalcogenide enriched cocatalysts. *Chem. Eng. J.* **2023**, *455*, 140601. [[CrossRef](#)]
95. Shruthi, B.; Madhu, B.J.; Bheema Raju, V.; Vynatheya, S.; Veena Devi, B.; Jayashree, G.V.; Ravikumar, C.R. Synthesis, spectroscopic analysis and electrochemical performance of modified bnickel hydroxide electrode with CuO. *J. Sci. Adv. Mater. Devices* **2016**, *2*, 93–98. [[CrossRef](#)]
96. Avinash, B.; Ravikumar, C.R.; Kumar, M.A.; Nagaswarupa, H.P.; Santosh, M.S.; Bhatt, A.S.; Kuznetsov, D. Nano CuO: Electrochemical sensor for the determination of paracetamol and D-glucose. *J. Phys. Chem. Solids* **2019**, *134*, 193–200. [[CrossRef](#)]
97. Ravikumar, C.R.; Kotteeswaran, P.; Bheema raju, V.; Murugan, A.; Santosh, M.S.; Nagaswarupa, H.P.; Prashantha, S.C.; Anil Kumar, M.R.; Shivakumar, M.S. Influence of zinc additive and pH on the electrochemical activities of β-nickel hydroxide materials and its applications in secondary batteries. *J. Energy Storage* **2017**, *9*, 12–24. [[CrossRef](#)]
98. Rashmi, B.N.; Harlapur, S.F.; Gurushantha, K.; Ravikumar, C.R.; Kumar, M.A.; Santosh, M.S.; Kumar, V.D.; Kumar, A.N.; Azad, A.K.; Murthy, H.A. Facile green synthesis of lanthanum oxide nanoparticles using Centella Asiatica and Tridax plants: Photocatalytic, electrochemical sensor and antimicrobial studies. *Appl. Surf. Sci. Adv.* **2022**, *7*, 100210. [[CrossRef](#)]
99. Nagarani, S.; Sasikala, G.; Yuvaraj, M.; Kumar, R.D.; Balachandran, S.; Kumar, M. ZnO–CuO Nanoparticles Enameled on Reduced Graphene Nanosheets as Electrode Materials for Supercapacitors. *J. Energy Storage* **2022**, *52*, 104969. [[CrossRef](#)]
100. Kumar, R.; Singh, B.K.; Soam, A.; Parida, S.; Sahajwalla, V.; Bhargava, P. In situ carbon-supported titanium dioxide (ICS–TiO<sub>2</sub>) as an electrode material for high performance supercapacitors. *Nanoscale Adv.* **2020**, *2*, 2376–2386. [[CrossRef](#)]
101. Li, Z.; Zhou, Z.; Yun, G.; Shi, K.; Lv, X.; Yang, B. High-performance Solid-state Supercapacitors Based on Graphene–ZnO Hybrid Nanocomposites. *Nanoscale Res. Lett.* **2013**, *8*, 473. [[CrossRef](#)]

**Disclaimer/Publisher’s Note:** The statements, opinions and data contained in all publications are solely those of the individual author(s) and contributor(s) and not of MDPI and/or the editor(s). MDPI and/or the editor(s) disclaim responsibility for any injury to people or property resulting from any ideas, methods, instructions or products referred to in the content.